aerospace

MDPI

Article

System-Constrained Multi-Gravity-Assist Trajectory Design for Small Satellites

Sumeth Daluwatta and Nishanth Pushparaj *

Department of Mechanical, Materials, and Manufacturing Engineering, University of Nottingham, Nottingham NG7 2RD, UK; egysd6@nottingham.ac.uk
* Correspondence: nishanth.pushparaj@nottingham.ac.uk

Abstract

Small-satellite mission design requires joint consideration of trajectory geometry, launch conditions, propulsion capacity, spacecraft mass, and operational lifetime. This study presents an integrated preliminary-design workflow combining Lambert-grid exploration, cascade filtering, and differential-evolution refinement, followed by encounter and spacecraft screening. The workflow is illustrated using Earth–Venus–Mars–Earth, Earth–Moon–Earth–Moon, and Earth–Venus–Earth–Vesta mission contexts. Launch-provided injection is separated from onboard manoeuvre requirements, and the optimization objective is identified as an energy-and-encounter-matching surrogate. An analytical assessment of 20 spacecraft–propulsion configurations shows that increasing the assumed total correction allowance from 0.10 to 0.40 km s^{-1} reduces capacity-compliant configurations from 18 to 15. For a fixed 1538-day benchmark, increasing the assumed 3.5-year microsatellite lifetime by approximately 20.3% removes its lifetime-only exclusion. A 5 kg Nano R3 configuration requires approximately 16.50 days of ideal powered operation to deliver 100 m s^{-1}, illustrating the distinction between propellant capacity and manoeuvre-time feasibility. The results show that the candidate configuration set depends materially on the adopted screening assumptions. The framework uses patched-conic dynamics and ideal propulsion screening; independent trajectory reconstruction, stochastic robustness assessment, and finite-thrust verification remain outstanding.

Keywords: small satellites; CubeSat; multi-gravity assist; gravity assist; trajectory optimization; Lambert problem; differential evolution; porkchop plot; electric propulsion; cislunar trajectory; Vesta

Check for updates

Academic Editor: Gang Zhang

Received: 15 August 2026
Revised: 19 September 2026
Accepted: 20 September 2026
Published: 26 September 2026

Copyright: © 2026 by the authors. Licensee MDPI, Basel, Switzerland. This article is an open access article distributed under the terms and conditions of the Creative Commons Attribution (CC BY) license.

1. Introduction

Small satellites have substantially broadened access to space science and technology demonstration by reducing spacecraft development cost, mass, and programmatic complexity relative to conventional large spacecraft [1]. Recent mission surveys show that CubeSat-class platforms are now being considered across an increasingly diverse range of Earth-orbiting, cislunar, planetary, and deep-space applications [2]. This progression is important for planetary exploration because universities, emerging space agencies, and comparatively small mission teams can potentially conduct focused scientific investigations without the cost and schedule associated with traditional flagship spacecraft.

The feasibility of deep-space small-satellite operations has already been demonstrated experimentally. NASA's Mars Cube One (MarCO) spacecraft accompanied the InSight mission to Mars and relayed entry, descent, and landing telemetry, demonstrating interplanetary

navigation, communications, and spacecraft operations with a 6U CubeSat platform [3]. Nevertheless, extension of this capability to independent interplanetary missions remains strongly influenced by spacecraft-level resource constraints. Propulsion systems compatible with CubeSat and SmallSat platforms typically trade high specific impulse against low thrust, limited propellant capacity, electrical-power demand, and stringent hardware-volume and mass constraints [4]. NASA's current state-of-the-art assessment likewise shows a rapidly developing but strongly system-dependent small-spacecraft propulsion landscape [5]. Consequently, trajectory design, launch architecture, power availability, propulsion integration, and spacecraft lifetime cannot be treated as independent considerations.

Gravity assists provide one mechanism for addressing this problem. During a planetary flyby, a spacecraft can exchange orbital energy and angular momentum with the encountered body, changing its heliocentric velocity vector without requiring an equivalent propulsive velocity increment [6]. This technique has been fundamental to major interplanetary missions, including Voyager and Galileo [7,8], and forms the basis of a substantial body of multi-gravity-assist trajectory-design research [9]. For a propulsion-limited small spacecraft, gravity assists are particularly attractive because large heliocentric energy changes can be obtained from encounter geometry rather than directly from onboard propellant.

However, the trajectory-design problem is highly nonlinear. For a prescribed sequence of bodies, the combination of launch epoch, individual-leg times-of-flight, planetary phasing, flyby altitude, incoming and outgoing hyperbolic-excess velocities, and terminal conditions creates a multimodal search space. Classical patched-conic methods and Lambert solutions remain highly effective for preliminary design [10,11], whereas global-optimization strategies are commonly used to explore the resulting non-convex design space [12]. Recent work continues to advance MGA optimization through improved search-space pruning [13], alternative formulations that avoid repeated direct use of Lambert solutions during global search [14], and hybrid sequence-generation and optimization approaches such as Tisserand-graph methods combined with evolutionary optimization [15]. These developments indicate that computational efficiency and reliable identification of globally competitive encounter sequences remain active areas of research.

For propulsion-limited spacecraft, an additional distinction is required between impulsive MGA design and true low-thrust trajectory optimization. Continuous low-thrust optimization has been extensively studied [16,17], with recent work demonstrating increasingly sophisticated numerical techniques for finite-thrust and constrained transfers [18]. Low-thrust resonance-gravity-assist design has also been investigated directly in the cislunar domain [19]. A recent broader review of orbit-transfer optimization highlights continued development of evolutionary, direct, indirect, convex, and data-driven trajectory-design methods [20]. These high-fidelity formulations are necessary for final mission design, but their computational cost and dependence on a suitable initial solution can make them less attractive during early architecture screening.

The present study addresses this preliminary-design need through an integrated workflow connecting multi-gravity-assist trajectory exploration with explicit spacecraft-level screening assumptions. The underlying techniques—Lambert solutions, trajectory filtering, differential evolution (DE), patched-conic encounter modelling, and rocket-equation calculations—are established methods [10,12,21]. The contribution lies in their coordinated application and in the explicit separation of trajectory-search objectives, launch-provided departure conditions, encounter feasibility, and spacecraft resource constraints. This study does not introduce a new Lambert solver or evolutionary optimization algorithm.

The workflow combines three computational stages: (i) Lambert-grid exploration of individual transfer legs; (ii) cascade filtering to retain approximately matched multi-leg candidates; and (iii) continuous refinement using DE, followed by encounter- and

spacecraft-level screening. Differential evolution provides a gradient-free search over the continuous design variables [21]. Approximate matching during candidate generation is distinguished from the physical acceptance conditions applied to the refined trajectories. Similarly, the trajectory-search objective is distinguished from the onboard manoeuvre requirement used in propulsion screening.

Relative to a preliminary trajectory search that ranks candidates using launch energy, transfer duration, or a propulsive cost alone, the present workflow additionally examines their compatibility with adopted propulsion capacity, spacecraft mass, correction allowances, and operational lifetime. The Earth–Venus–Mars–Earth (EVME), Earth–Moon–Earth–Moon, and Earth–Venus–Earth–Vesta cases provide contrasting mission contexts, spanning a planetary free-return scenario, short-duration cislunar flight, and a long-duration main-belt transfer. This comparison is intended to identify which screening assumptions constrain the candidate architecture set and how changes in those assumptions affect its composition. The resulting configurations are conditional candidates for further investigation; they do not establish global optimality, finite-thrust feasibility, or a complete spacecraft design.

The specific contributions of this study are as follows:

1. A structured preliminary-design workflow linking broad Lambert-grid exploration, multi-leg candidate filtering, and continuous trajectory refinement, with a distinction between search-stage tolerances and final encounter-acceptance conditions.
2. Explicit separation of launch-provided Earth-departure conditions from onboard manoeuvre requirements, allowing propulsion capacity to be assessed against a stated correction allowance and any separately modelled deterministic manoeuvres.
3. A cross-mission assessment of how adopted propulsion, spacecraft-mass, and operational-lifetime assumptions affect the candidate architecture set, with the resulting conclusions interpreted within the scope of the screening model.

Small-body operations by CubeSat-class spacecraft are already the subject of detailed trajectory-design studies, including missions such as Milani [22]; the present work instead focuses on the preceding heliocentric or geocentric transfer architecture and its compatibility with the resource limitations of small spacecraft.

2. Problem Formulation

2.1. Dynamical Model and Mission Assumptions

The objective is to identify a set of encounter epochs and leg times-of-flight that produce a physically admissible MGA trajectory while remaining compatible with a representative small-satellite architecture. The analysis is performed at preliminary-design fidelity using the patched-conic approximation [10,11]. Each interplanetary leg is therefore represented as a two-body heliocentric conic, while a planetary encounter is represented by a local hyperbolic flyby. The cislunar case is formulated in an Earth-centred two-body frame.

The analysis adopts a patched-conic dynamical model in which the spacecraft is assumed to be influenced by a single dominant gravitational body during each transfer leg, with transitions between planetary and heliocentric regimes treated instantaneously. Planetary encounters are modelled as instantaneous flybys, while all trajectory manoeuvres are represented impulsively. Each transfer leg is therefore propagated under point-mass central-body gravity, which is appropriate for preliminary trajectory design but does not capture higher-order dynamical effects.

Non-gravitational perturbations, including solar-radiation pressure and atmospheric drag, together with third-body perturbations outside the active central-body model, are neglected during the Lambert search. Minimum-periapsis constraints are imposed to reject transfer arcs or flyby geometries that would intersect the central body or violate the adopted safe-altitude limits. The baseline mission architecture further assumes rideshare injection,

such that the launch vehicle provides the initial Earth-departure energy. Propulsion-system feasibility is assessed only after trajectory refinement using the available ΔV, spacecraft mass, and operational-lifetime constraints; continuous finite-thrust arcs are not propagated within the optimization.

The model should therefore be interpreted as an architecture-screening model rather than a navigation-grade trajectory propagator. In particular, the use of an electric-propulsion system in the spacecraft trade study does not convert the underlying trajectory model into a continuous low-thrust optimization. Finite-burn steering losses, thrust-direction histories, eclipse-related thrust interruptions, detailed power-system performance, and navigation-correction dispersions are outside the present formulation. Such effects can be incorporated in a subsequent high-fidelity phase using direct or convex low-thrust methods [16,23] and more recent finite-thrust formulations [18].

2.2. Mission Design Variables

For a mission consisting of N transfer legs, the design vector is written as

$$\mathbf{x} = [t_0, T_1, T_2, \ldots, T_N], \tag{1}$$

where t_0 is the initial departure epoch and T_k is the time-of-flight of leg k. Under the instantaneous patched-conic encounter assumption, subsequent encounter epochs are reconstructed as

$$t_k = t_0 + \sum_{j=1}^{k-1} T_j, \qquad k = 2, \ldots, N. \tag{2}$$

This representation eliminates the need to optimize each encounter date independently and imposes chronological continuity directly through the leg durations.

For each leg, the positions of the departure and arrival bodies are

$$\mathbf{r}_{1,k} = \mathbf{r}_{B_k}(t_k) \tag{3}$$

and

$$\mathbf{r}_{2,k} = \mathbf{r}_{B_{k+1}}(t_k + T_k). \tag{4}$$

The Lambert problem is then solved as

$$(\mathbf{v}_{1,k}, \mathbf{v}_{2,k}) = \mathcal{L}(\mathbf{r}_{1,k}, \mathbf{r}_{2,k}, T_k, \mu), \tag{5}$$

where $\mathcal{L}$ represents the Lambert solver, $\mathbf{v}_{1,k}$ and $\mathbf{v}_{2,k}$ are the transfer-orbit velocities at the beginning and end of the leg, and μ is the gravitational parameter of the central body.

2.3. Characteristic Energy and Hyperbolic-Excess Velocity

For heliocentric interplanetary transfers, the departure hyperbolic-excess-velocity vector is

$$\mathbf{v}_{\infty,k}^{\mathrm{dep}} = \mathbf{v}_{1,k} - \mathbf{v}_{B_k}(t_k), \tag{6}$$

and the corresponding departure characteristic energy is

$$C_{3,k} = \left\| \mathbf{v}_{\infty,k}^{\mathrm{dep}} \right\|^2. \tag{7}$$

Similarly, the arrival hyperbolic-excess velocity is

$$\mathbf{v}_{\infty,k}^{\mathrm{arr}} = \mathbf{v}_{2,k} - \mathbf{v}_{B_{k+1}}(t_k + T_k), \tag{8}$$

with magnitude

$$v_{\infty,k}^{\mathrm{arr}} = \left\| \mathbf{v}_{\infty,k}^{\mathrm{arr}} \right\|. \tag{9}$$

The conventional C_3 quantity has a direct hyperbolic-escape interpretation when the spacecraft is departing a planet into an unbound asymptote. The cislunar case remains geocentrically bound in the solutions investigated here. To avoid conflating the two interpretations, the signed quantity used in the original cislunar computation is denoted here by C_3^*:

$$C_3^* = \|\mathbf{v}_{\mathrm{sc}}\|^2 - v_{\mathrm{esc}}^2 = \|\mathbf{v}_{\mathrm{sc}}\|^2 - \frac{2\mu_E}{r}. \tag{10}$$

A negative value of C_3^* indicates that the trajectory is bound with respect to Earth within the adopted geocentric two-body approximation.

2.4. Gravity-Assist Conditions

Within the instantaneous patched-conic approximation, a gravity assist connects the incoming and outgoing transfer legs at a common encounter epoch t_p. The corresponding hyperbolic-excess-velocity vectors are defined as

$$\begin{aligned} \mathbf{v}_\infty^- &= \mathbf{v}_{\mathrm{sc}}^-(t_p) - \mathbf{v}_p(t_p), \\ \mathbf{v}_\infty^+ &= \mathbf{v}_{\mathrm{sc}}^+(t_p) - \mathbf{v}_p(t_p), \end{aligned} \tag{11}$$

where $\mathbf{v}_{\mathrm{sc}}^-$ and $\mathbf{v}_{\mathrm{sc}}^+$ are the terminal and initial velocities of the adjacent transfer legs, respectively, and $\mathbf{v}_p$ is the velocity of the encountered body. All vectors are expressed in the same inertial reference frame. The superscripts $-$ and $+$ denote the incoming and outgoing asymptotes of the planetocentric hyperbolic trajectory.

For an ideal unpowered encounter in the planetocentric two-body model, conservation of specific orbital energy requires equal incoming and outgoing asymptotic speed magnitudes [10]:

$$\left\|\mathbf{v}_\infty^-\right\| = \left\|\mathbf{v}_\infty^+\right\| = v_\infty. \tag{12}$$

This equality concerns the asymptotic speeds and does not imply constant local speed throughout the flyby. At a finite planetocentric distance r, the local speed is

$$v(r) = \sqrt{v_\infty^2 + \frac{2\mu_p}{r}}, \tag{13}$$

where μ_p is the gravitational parameter of the encountered body. The spacecraft therefore accelerates during approach and decelerates during departure. Under the same ideal assumptions, local speeds at incoming and outgoing points with equal planetocentric radii are also equal, including equal-radius sphere-of-influence boundaries.

Independently sampled Lambert legs generally do not satisfy Equation (12) exactly. Their excess-speed matching residual is defined as

$$\Delta v_\infty = \left| \left\|\mathbf{v}_\infty^-\right\| - \left\|\mathbf{v}_\infty^+\right\| \right|. \tag{14}$$

This quantity measures imperfect matching between candidate legs; it does not represent a physical violation of energy conservation. Coarse filtering may retain approximately matched candidates for continuous refinement, but this preliminary retention must be distinguished from final acceptance as an unpowered flyby.

The required angular deflection between the incoming and outgoing planet-relative asymptotic velocity vectors is

$$\delta_{\text{req}} = \cos^{-1}\left[\frac{\mathbf{v}_\infty^- \cdot \mathbf{v}_\infty^+}{\|\mathbf{v}_\infty^-\|\|\mathbf{v}_\infty^+\|}\right]. \tag{15}$$

For a speed-matched unpowered hyperbola, the turning angle increases as the periapsis radius decreases. Consequently, the maximum permissible turning angle for a prescribed minimum periapsis radius $r_{p,\min}$ is

$$\delta_{\max} = 2\sin^{-1}\left[\frac{1}{1 + r_{p,\min} v_\infty^2/\mu_p}\right], \tag{16}$$

where $r_{p,\min} = R_p + h_{p,\min}$, R_p is the adopted body radius, and $h_{p,\min}$ is the minimum permitted flyby altitude.

Final numerical acceptance of each intermediate unpowered encounter requires

$$\Delta v_\infty \le \varepsilon_v, \qquad \delta_{\text{req}} \le \delta_{\max}, \tag{17}$$

where ε_v is the final excess-speed matching tolerance, distinct from any more permissive threshold used during candidate generation. This tolerance represents numerical matching accuracy and is not an additional onboard manoeuvre allowance. A candidate that fails either condition requires further refinement or explicit modelling of a powered encounter. In particular, the scalar residual Δv_∞ alone does not constitute a complete powered-flyby manoeuvre calculation.

The screening model adopts minimum flyby altitudes of 200 km at Venus and Mars, 400 km at Earth, and 100 km at the Moon. These are preliminary-design values and should not be interpreted as final navigation or planetary-protection constraints.

2.5. Mission Duration and Earth-Return Constraint

The transfer duration is

$$T_{\text{mission}} = \sum_{k=1}^{N} T_k. \tag{18}$$

For free-return trajectories terminating at Earth, the atmospheric-entry speed is estimated from the geocentric hyperbolic-excess velocity using

$$v_{\text{entry}} = \sqrt{v_{\infty,E}^2 + v_{\text{esc},E}^2}, \tag{19}$$

where $v_{\text{esc},E} = 11.18\,\text{km}\,\text{s}^{-1}$ is used in the original screening model. A preliminary maximum entry speed of $12\,\text{km}\,\text{s}^{-1}$ is imposed.

2.6. Launch-Vehicle Energy and Onboard Spacecraft ΔV

A central feature of the problem formulation is the separation between characteristic energy supplied by the launch system and velocity change supplied by the spacecraft.

For departure from a circular Earth parking orbit of radius r_0, the ideal impulsive velocity increment corresponding to a prescribed geocentric characteristic energy C_3 is

$$\Delta V_{\text{dep}} = \sqrt{C_3 + \frac{2\mu_E}{r_0}} - \sqrt{\frac{\mu_E}{r_0}}. \tag{20}$$

This estimate assumes tangential injection at the parking-orbit radius and compatible departure geometry. It does not include losses associated with finite-duration thrusting or additional manoeuvres required to establish the departure orientation.

In the baseline rideshare scenario, the launch service is assumed to supply the nominal initial state required by the first transfer leg. For the interplanetary cases, this includes the departure epoch and outgoing Earth-relative asymptote, with its associated C_3. For the cislunar case, it denotes injection into the prescribed Earth-centred transfer, which need not be an Earth-escape trajectory. Accordingly, the nominal first-leg injection is excluded from the onboard spacecraft budget:

$$\Delta V_{\mathrm{SC},1} = 0. \tag{21}$$

This is a conditional launch-architecture assumption. Compatibility with a particular rideshare opportunity requires agreement in departure epoch, energy, and direction; a suitable scalar C_3 alone is insufficient. Equation (21) concerns the nominal injection and does not imply that post-separation trajectory corrections are unnecessary. Related work has investigated transfers from geostationary transfer orbits through Earth-synchronous orbits and subsequent Earth gravity assists to expand interplanetary departure opportunities for piggyback spacecraft [24]. Such strategies explicitly connect the launch-provided orbit to the interplanetary departure conditions, illustrating the importance of accounting for the transfer between these states.

The correction allowance is therefore specified separately from the nominal transfer geometry. The adopted baseline allocation per intermediate encounter is

$$q \equiv \Delta V_{\mathrm{TCM}} = 0.05\ \mathrm{km\,s^{-1}}. \tag{22}$$

Each mission sequence contains three transfer legs and two intermediate encounters. The corresponding nominal onboard screening requirement is therefore

$$\Delta V_{\mathrm{SC}} = 2q = 2\Delta V_{\mathrm{TCM}} = 0.10\ \mathrm{km\,s^{-1}}. \tag{23}$$

The value of q is an illustrative preliminary-design assumption rather than a navigation-derived prediction or a demonstrated upper bound on correction requirements. Actual requirements depend on launch-injection dispersion, orbit-determination accuracy, encounter-targeting requirements, manoeuvre execution errors, and the propagation of uncertainty between encounters. A common baseline allocation provides a consistent reference for comparing the adopted propulsion configurations, but it does not imply equal navigation difficulty across the three missions. The allocation must therefore be treated as a screening parameter whose influence on the candidate architecture set requires assessment.

Any deterministic manoeuvre required by the nominal trajectory must be added explicitly to the correction allowance. More generally, the onboard requirement is

$$\Delta V_{\mathrm{SC,req}} = \Delta V_{\mathrm{SC},1} + \sum_j \Delta V_{\mathrm{det},j} + 2q, \tag{24}$$

where $\Delta V_{\mathrm{det},j}$ denotes the magnitude of an explicitly modelled deterministic manoeuvre, such as a deep-space manoeuvre, powered flyby, or terminal rendezvous or orbit-insertion manoeuvre. The nominal value in Equation (23) corresponds to the rideshare assumption, with no additional deterministic manoeuvres included in the transfer model.

The correction reserve cannot be used implicitly to compensate for an encounter that fails the unpowered-flyby conditions. In particular, a nonzero excess-speed mismatch between adjacent Lambert legs is a matching residual; it is not automatically an executable manoeuvre of the same magnitude. Such a candidate requires further refinement or explicit powered-encounter modelling before its onboard requirements can be assessed.

This separation allows launch energy and onboard correction capacity to be examined as distinct design quantities. The resulting propulsion-screening conclusions remain con-

ditional on the assumed launch-provided initial state, correction allocation, and terminal mission requirements.

2.7. Propulsion and Spacecraft Feasibility

The available impulsive-equivalent ΔV of a candidate propulsion architecture is estimated using the Tsiolkovsky rocket equation:

$$\Delta V_{\text{budget}} = I_{\text{sp}} g_0 \ln\left(\frac{m_0}{m_f}\right), \tag{25}$$

or, in terms of propellant mass fraction η,

$$\Delta V_{\text{budget}} = I_{\text{sp}} g_0 \ln\left(\frac{1}{1-\eta}\right), \qquad \eta = \frac{m_p}{m_0}, \tag{26}$$

where I_{sp} is the specific impulse, $g_0 = 9.80665 \times 10^{-3}\,\text{km}\,\text{s}^{-2}$, m_p is the propellant mass, and m_0 is the spacecraft wet mass.

At this screening level, propulsion feasibility requires

$$\Delta V_{\text{budget}} \geq \Delta V_{\text{SC}}, \tag{27}$$

in addition to compatibility between the propulsion hardware and spacecraft mass.

Seven representative electric-propulsion systems are considered over a set of spacecraft masses spanning the small-satellite regime. The propulsion technologies and numerical parameters adopted in the architecture trade study are summarised in Table 1. The dataset includes the ENPULSION Nano R3, ThrustMe NPT30-I2, Busek BIT-3, Exotrail spaceware Nano and Micro systems, and the Busek BHT-100 and BHT-200 [25–30].

Table 1. Representative small-satellite propulsion systems considered in the spacecraft architecture trade study.

System	Type	I_{sp} (s)	Thrust (mN)	Propellant Mass (kg)	Dry Mass (kg)	Spacecraft Mass Range (kg)
ENPULSION Nano R3 [25]	FEEP	2500	0.35	0.215	1.28	1–10
ThrustMe NPT30-I2 [26,31]	Gridded ion	2450	1.10	0.229	1.00	10–25
Busek BIT-3 [27]	RF ion	2150	1.10	1.50	1.40	25–50
Exotrail spaceware Nano [28]	Hall effect	1200	2.50	0.510	1.50	50–80
Busek BHT-100 [29]	Hall effect	1000	7.00	4.62	2.00	80–100
Exotrail spaceware Micro [28]	Hall effect	1500	7.00	4.08	3.00	100–150
Busek BHT-200 [30]	Hall effect	1390	13.0	10.27	2.50	150–180

Note: Propulsion parameters were adopted from manufacturer data [25–30]. The spacecraft mass ranges correspond to the architecture ranges used in the present feasibility study.

The hardware values are treated as the fixed design dataset used to generate the reported results, rather than as a procurement survey of currently available products. This distinction is important because commercial SmallSat propulsion technology evolves rapidly; the 2026 NASA state-of-the-art survey provides a current overview of commercially available and emerging propulsion technologies [5].

Operational lifetime is represented using an assumed screening limit associated with spacecraft wet mass. The nominal limits are

$$L_0(m_0) = \begin{cases} 1.5\ \text{yr}, & m_0 \leq 10\ \text{kg}, \\ 3.5\ \text{yr}, & 10\ \text{kg} < m_0 \leq 100\ \text{kg}, \\ 6.0\ \text{yr}, & m_0 > 100\ \text{kg}. \end{cases} \tag{28}$$

These intervals provide the nanosatellite, microsatellite, and minisatellite groupings used in the present screening model. Lifetime compliance requires the elapsed mission duration, expressed in years, to remain within the applicable limit.

The numerical limits are adopted scenario assumptions rather than universal physical limits or predictions of spacecraft survival. Spacecraft mass is used to assign the screening category; it does not determine operational lifetime by itself. Actual lifetime capability depends on component qualification, radiation exposure, power degradation, thermal cycling, consumables, redundancy, communications, and mission operations. These effects are not resolved individually in the present model.

The purpose of the class-level limits is to provide a transparent baseline for examining the influence of mission duration on the candidate architecture set. Their effect is therefore assessed through the sensitivity analysis in Section 5.6, rather than treating the nominal boundaries as established limits on small-spacecraft capability.

3. Computational Methodology

The proposed computational framework is organised into three sequential stages, as summarised in Figure 1: The first stage performs a broad Lambert-grid search over the prescribed departure and arrival windows for each individual trajectory leg, generating porkchop maps and retaining candidate transfers that satisfy the initial energy, time-of-flight, and periapsis constraints. The second stage connects the independently generated legs through a cascade-filtering process, enforcing temporal continuity, compatibility of the incoming and outgoing hyperbolic-excess velocities, launch-energy constraints, and preliminary flyby and Earth-entry feasibility. The resulting multi-leg trajectories provide physically informed initial conditions for the third stage, in which differential evolution refines the departure epoch and individual-leg times-of-flight.

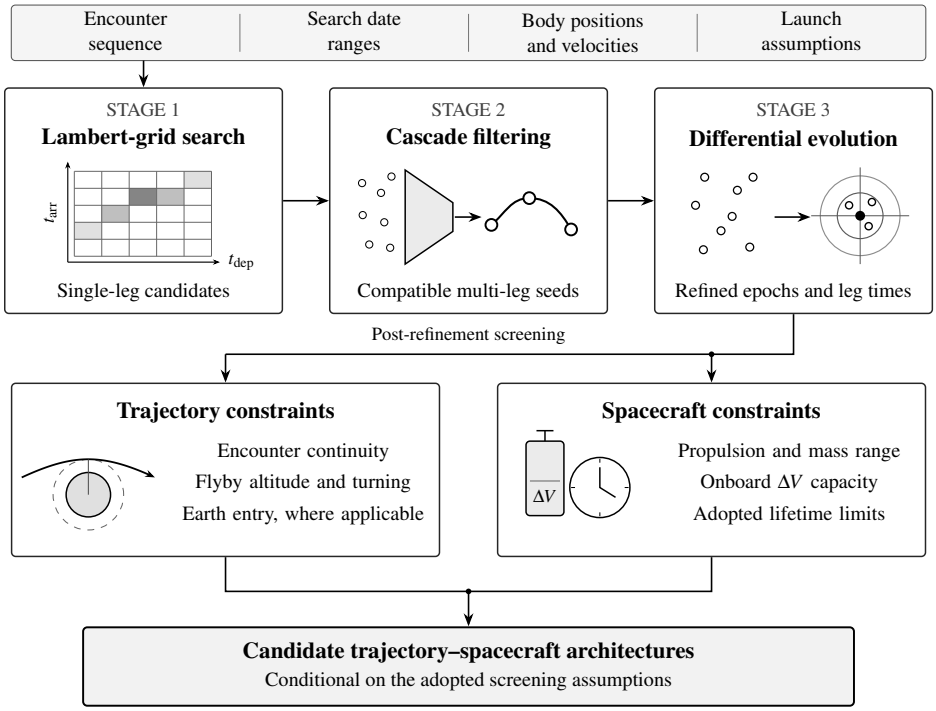


Figure 1. Three-stage preliminary-design workflow for system-constrained multi-gravity-assist trajectories. Lambert-grid exploration generates single-leg candidates, cascade filtering assembles compatible multi-leg seeds, and differential evolution refines the departure epoch and leg times-of-flight. The refined trajectories are then assessed against trajectory and spacecraft constraints to identify candidate architectures under the adopted screening assumptions. The sketches are schematic.

Following trajectory refinement, the optimized solution is subjected to two complementary system-level assessments: The trajectory-feasibility branch evaluates the flyby periapsis, available turning-angle capability, Earth-entry speed (where applicable), and overall mission duration. In parallel, the spacecraft-screening branch assesses propulsion-system compatibility, Tsiolkovsky ΔV capability, spacecraft mass range, and representative operational lifetime. The final output is therefore not only an optimized MGA trajectory but a trajectory–spacecraft architecture that satisfies the feasibility criteria adopted for the preliminary mission design.

As shown in Figure 1, the framework deliberately separates trajectory generation and optimization from spacecraft-level feasibility assessment. This separation allows the trajectory search to explore the available encounter geometry without prematurely restricting the solution to a particular propulsion system, while the subsequent screening stage determines whether the resulting trajectory can be supported by a representative small-satellite platform. The following subsections describe each stage of the framework in detail.

The computational sequence implemented in the framework is summarised in Algorithm 1. The algorithm provides the procedural link between the individual trajectory-search stages and the final spacecraft-level feasibility assessment.

3.1. Stage 1: Lambert-Grid and Porkchop-Plot Search

The first stage performs a grid search over the departure and arrival epochs of each transfer leg. Planetary positions and velocities are obtained using MATLAB 2025b planetary ephemerides. For the Vesta case, heliocentric asteroid states are taken from JPL Horizons and cached before the trajectory sweep.

Interplanetary legs are computed in a heliocentric frame using

$$\mu_{\odot} = 1.3271244 \times 10^{11}\ \mathrm{km^3\,s^{-2}}, \tag{29}$$

whereas the cislunar problem is computed in a geocentric frame using

$$\mu_E = 398600.4418\ \mathrm{km^3\,s^{-2}}. \tag{30}$$

Each departure–arrival pair is evaluated by solving Lambert's boundary-value problem. Both short- and long-way transfer possibilities are evaluated where applicable, and the candidate with the preferred energy measure is retained. The transfer angle is calculated from

$$\nu = \cos^{-1}\left[\frac{\mathbf{r}_1 \cdot \mathbf{r}_2}{\|\mathbf{r}_1\|\|\mathbf{r}_2\|}\right]. \tag{31}$$

The Lambert implementation follows an Izzo-type approach consistent with methods widely used for large-scale MGA searching [12]. Recent trajectory-optimization work has developed alternatives that reduce or avoid explicit repeated Lambert evaluation during global MGA optimization [14]; however, the direct grid approach remains attractive here because the porkchop maps also provide a transparent physical interpretation of the candidate launch and encounter windows.

A periapsis filter rejects a transfer conic if its computed periapsis lies below the surface of the relevant central body. For each retained transfer, the algorithm stores departure epoch, arrival epoch, C_3 (or C_3^* for the cislunar problem), departure and arrival v_∞, and time-of-flight.

The interplanetary and asteroid searches use a nominal one-day grid. A 0.5-day grid is used for the cislunar problem because the relative Earth–Moon geometry evolves significantly over the Moon's orbital period. MATLAB parallelization is used to distribute independent Lambert evaluations across the available processing cores.

Mission-specific screening is applied before export. An upper C_3 limit removes excessively energetic solutions, while the cislunar resonant leg is constrained to a physically relevant time-of-flight interval. The output of Stage 1 is therefore a set of independent feasible-leg databases rather than complete trajectories.

Algorithm 1 Three-stage MGA trajectory search and spacecraft feasibility framework

Require: Body sequence $\mathcal{B}$, search windows, $C_{3,\max}$, ϵ_t, ϵ_{v_∞}, $r_{p,\min}$, $v_{\text{entry,max}}$, propulsion database $\mathcal{P}$
Ensure: Optimized trajectory $\mathbf{x}^*$ and feasible architectures $\mathcal{A}$

Stage 1: Lambert grid search
for $k = 1$ to N **do**
  $\mathcal{D}_k \leftarrow \emptyset$
  for all $(t_{\text{dep}}, t_{\text{arr}})$ in search grid **do**
    Obtain departure and arrival ephemerides
    $(\mathbf{v}_1, \mathbf{v}_2) \leftarrow \text{Lambert}(\mathbf{r}_1, \mathbf{r}_2, T_k, \mu)$
    if solution converges and satisfies periapsis, C_3, and TOF limits **then**
      Compute C_3, v_∞^{dep}, v_∞^{arr}, and T_k
      $\mathcal{D}_k \leftarrow \mathcal{D}_k \cup \{\text{candidate}\}$
    end if
  end for
end for
Stage 2: Cascade filtering
Initialise trajectory chains $\mathcal{C}$ from $\mathcal{D}_1$
for $k = 2$ to N **do**
  for all $c \in \mathcal{C}$ and $d \in \mathcal{D}_k$ **do**
    if $|\Delta t| \le \epsilon_t$ **and** $\Delta v_\infty \le \epsilon_{v_\infty}$ **then**
      Compute δ_{req} and $\delta_{\max}$
      if $\delta_{\text{req}} \le \delta_{\max} + \epsilon_\delta$ **then**
        if Earth return **then**
          Retain only if $v_{\text{entry}} \le v_{\text{entry,max}}$
        else
          Retain connected trajectory
        end if
      end if
    end if
  end for
end for
Rank complete trajectories and retain the best K seeds
Stage 3: Differential evolution
Form $\mathbf{x} = [t_0, T_1, \ldots, T_N]$ and initialise population from ranked seeds
for $g = 1$ to N_g **do**
  for $i = 1$ to N_p **do**
    Select distinct $r_1, r_2, r_3 \neq i$
    $\mathbf{m}_i \leftarrow \mathbf{x}_{r_1} + F(\mathbf{x}_{r_2} - \mathbf{x}_{r_3})$
    $\mathbf{u}_i \leftarrow \text{Crossover}(\mathbf{x}_i, \mathbf{m}_i, CR)$
    if $J(\mathbf{u}_i) < J(\mathbf{x}_i)$ **then**
      $\mathbf{x}_i \leftarrow \mathbf{u}_i$
    end if
  end for
end for
$\mathbf{x}^* \leftarrow \arg\min_{\mathbf{x}_i} J(\mathbf{x}_i)$
Post-optimization screening
Evaluate flyby geometry, v_∞ continuity, entry speed, and mission duration
$\mathcal{A} \leftarrow \emptyset$
for all compatible spacecraft-propulsion combinations (m, p) **do**
  Compute $\Delta V_{\text{budget}} = I_{\text{sp}} g_0 \ln(1/(1-\eta))$
  if $\Delta V_{\text{budget}} \ge \Delta V_{\text{SC}}$ **and** $T_{\text{mission}} \le T_{\text{life}}$ **then**
    $\mathcal{A} \leftarrow \mathcal{A} \cup \{(m, p)\}$
  end if
end for
return $\mathbf{x}^*, \mathcal{A}$

3.2. Stage 2: Multi-Leg Cascade Filtering

The second stage joins the individual leg databases into complete encounter chains. Each candidate connection must satisfy four classes of conditions:

1. Temporal continuity between the arrival of leg k and departure of leg $k+1$;
2. Compatibility of incoming and outgoing v_∞ magnitudes;
3. An allowable first-leg launch C_3;
4. Gravity-assist and, where appropriate, Earth-entry feasibility.

A one-day date tolerance is used to account for the discretization of the grid. The initial v_∞ tolerance is deliberately broad, at $10\,\mathrm{km\,s^{-1}}$, because this stage is intended to generate diverse seeds rather than to impose final encounter continuity. Candidate trajectories are subsequently tightened by the continuous optimizer.

The baseline cascade search restricts first-leg launch energy to

$$C_{3,\mathrm{launch}} \leq 20\,\mathrm{km^2\,s^{-2}} \tag{32}$$

for the EVME configuration. Flyby screening uses the gravitational parameter, body radius, and minimum flyby altitude to estimate the maximum available deflection. A 5° margin was allowed during the coarse cascade stage to avoid eliminating potentially useful seeds solely because of the one-day discretization.

The candidate score takes the general form

$$S = \sum_{k=1}^{N} w_k C_{3,k}, \tag{33}$$

with lower scores preferred. The original EVME implementation used the weighting vector

$$\mathbf{w} = [0.5,\ 0.3,\ 0.2] \tag{34}$$

for its three transfer legs, while additional weighting terms were available in the implementation for mission-dependent constraints.

The cascade-filter concept is related to the broader principle of reducing a large MGA search space before expensive continuous optimization [12]. Search-space pruning remains an active area of MGA research, with recent work demonstrating substantial improvements in convergence efficiency when physically motivated pruning is performed before global optimization [13].

The number of retained trajectory seeds is mission-dependent and must be distinguished from both the DE population size and the random seed used to initialise a stochastic optimization run. Retained trajectory seeds represent candidate regions identified by the cascade search; the DE random seed controls the subsequent random-number sequence. The retained candidate count is therefore reported separately for each mission. A larger candidate pool can improve coverage of distinct trajectory regions but does not necessarily improve the final solution if the additional candidates are redundant or of poor quality. No universal optimal number of retained seeds is established by the present study.

3.3. Stage 3: Differential-Evolution Refinement

The continuous refinement stage uses the DE/rand/1/bin strategy [21]. For three distinct population members $\mathbf{x}_{r_1}$, $\mathbf{x}_{r_2}$, and $\mathbf{x}_{r_3}$, a mutant vector is generated as

$$\mathbf{u} = \mathbf{x}_{r_1} + F(\mathbf{x}_{r_2} - \mathbf{x}_{r_3}), \tag{35}$$

where F is the mutation scale. Binomial crossover combines components of the mutant and target vectors using crossover probability CR to construct a trial vector.

The mission-specific baseline configurations are

$$(N_p, N_g) = \begin{cases} (100, 150), & \text{EVME}, \\ (80, 100), & \text{cislunar and Vesta}, \end{cases} \qquad (36)$$
$$F = 0.8, \qquad CR = 0.9,$$

where N_p is the population size and N_g is the generation limit. These are nominal algorithm configurations; their use does not establish that they are optimal for the mission cases.

Search bounds are constructed around the departure epochs and leg durations represented in the retained cascade candidates. The initial population incorporates the highest-ranked available trajectory seeds, with unfilled population positions generated randomly within the search bounds. All population members must satisfy the declared variable bounds. Approximate encounter matching at initialisation is distinguished from final acceptance of a physically admissible trajectory. Table 2 summarises the mission-specific search settings and the information available from the archived implementation and candidate files. The retained cascade-candidate count is distinct from the DE population size. The initial population uses the highest-ranked retained candidates up to the population limit; any remaining positions are filled randomly within the search bounds.

Table 2. Mission-specific DE settings and archived reproducibility information.

Quantity	EVME	Cislunar	Vesta
Population size, N_p	100	80	80
Generation limit, N_g	150	100	100
Mutation scale, F	0.8	0.8	0.8
Crossover probability, CR	0.9	0.9	0.9
Retained cascade candidates	27	24	2134
Initial members from cascade candidates	27	24	80
Randomly generated initial members	73	56	0

The original executions did not explicitly prescribe and archive the initial random-number-generator state or record elapsed computational time. These quantities therefore cannot be reconstructed reliably from the saved results. The reported settings document the search configuration but do not permit exact stochastic replay of the original executions or establish computational-performance comparisons between mission cases.

3.3.1. Optimization Cost Function

Differential evolution refines the departure epoch and individual leg durations using an energy-and-encounter-matching surrogate. This objective ranks candidate transfer geometries; it is not equivalent to total onboard manoeuvre demand, propellant consumption, or a finite-thrust mission cost.

For leg k, the departure hyperbolic-excess velocity is

$$\mathbf{v}_{\infty,k}^{\text{dep}} = \mathbf{v}_{1,k} - \mathbf{v}_{B_k}(t_k), \qquad (37)$$

where $\mathbf{v}_{B_k}(t_k)$ is the velocity of the departure body at the corresponding epoch. At an intermediate encounter, $\mathbf{v}_{\infty,k-1}^{\text{arr}}$ denotes the incoming excess-velocity vector from the preceding leg. Incoming and outgoing encounter quantities must be evaluated in a common reference frame and at the same encounter epoch.

The search objective takes the form

$$\begin{aligned} J(\mathbf{x}) = & \sum_{k=1}^{N} \left\| \mathbf{v}_{\infty,k}^{\mathrm{dep}} \right\|^2 \\ & + w_{\infty} \sum_{k=2}^{N} \left(\left\| \mathbf{v}_{\infty,k-1}^{\mathrm{arr}} \right\| - \left\| \mathbf{v}_{\infty,k}^{\mathrm{dep}} \right\| \right)^2 \\ & + P_{\mathrm{entry}} + P_{\mathrm{invalid}}, \end{aligned} \tag{38}$$

with $w_{\infty} = 50$. Velocity quantities in this objective are evaluated in $\mathrm{km\,s^{-1}}$. The first term penalises large departure excess speeds, while the second penalises imperfect matching of the incoming and outgoing excess-speed magnitudes.

For Earth free-return trajectories, the entry penalty is

$$P_{\mathrm{entry}} = \begin{cases} 1000 \left(v_{\mathrm{entry}} - v_{\mathrm{entry,max}} \right)^2, & v_{\mathrm{entry}} > v_{\mathrm{entry,max}}, \\ 0, & v_{\mathrm{entry}} \leq v_{\mathrm{entry,max}}, \end{cases} \tag{39}$$

where $v_{\mathrm{entry,max}} = 12\ \mathrm{km\,s^{-1}}$. For mission cases without the Earth-entry condition, $P_{\mathrm{entry}} = 0$.

The invalid-state penalty is used to reject failed Lambert evaluations and inadmissible transfer conics. Invalid candidates receive a large numerical penalty of 10^6; when a Lambert solution is unavailable, the remaining velocity-dependent terms cannot be evaluated and the rejection cost is assigned directly. The penalty coefficients are numerical search parameters and do not represent physical manoeuvre costs.

A reduction in J indicates improvement according to the adopted surrogate. It does not demonstrate a reduction in the spacecraft correction requirement or establish a minimum-ΔV trajectory. In particular, changes in launch energy and encounter matching can offset one another within the objective. The onboard requirement is assessed separately using the launch and manoeuvre accounting in Equation (24).

3.3.2. Search-Parameter Interpretation and Final Acceptance

The search parameters have distinct roles. Lambert-grid spacing controls the initial coverage of the departure and arrival domains. Cascade tolerances determine which approximately matched candidates are retained. The number of retained trajectory seeds affects coverage of candidate regions, whereas the DE population size, mutation scale, crossover probability, and generation limit govern the subsequent stochastic refinement.

A finer grid increases the number of sampled opportunities and the computational expense but does not by itself establish convergence of the final mission solution. Conversely, continuous refinement cannot guarantee recovery of a solution region that is absent from the retained candidates. Permissive cascade tolerances may preserve candidates that can become admissible after refinement, while restrictive tolerances reduce the refinement workload at the risk of discarding such candidates. These trade-offs motivate separate assessments of grid resolution, retained candidate count, and cascade thresholds.

The baseline values of F and CR are heuristic search settings rather than experimentally established optima. Multiple independent runs with recorded random seeds are required to quantify repeatability. Comparisons intended to isolate the effect of initialisation or an algorithm parameter require common search bounds, physical acceptance criteria, and a clearly stated computational budget.

Final physical acceptance is evaluated separately from the surrogate objective. Each intermediate unpowered encounter must satisfy the excess-speed matching and turning conditions in Equation (17). Applicable launch, terminal, and mission-duration constraints

must also be satisfied. A small objective value or termination of the optimizer is therefore insufficient to establish feasibility.

The resulting solutions are interpreted as candidates identified within the explored search domain. Global optimality and stochastic convergence reliability cannot be inferred from a single optimization run.

3.4. Post-Optimization Spacecraft Screening

The refined trajectory is evaluated against the compatible spacecraft–propulsion architectures. Under the adopted rideshare assumption, the nominal first-leg injection is supplied by the launch service. The baseline correction allocation is $q = 0.05\ \mathrm{km\,s^{-1}}$ per intermediate encounter, giving $2q = 0.10\ \mathrm{km\,s^{-1}}$ for each three-leg sequence. Any explicitly modelled deterministic manoeuvres must be added according to Equation (24). This allocation is a preliminary screening assumption and does not establish navigation or finite-thrust feasibility.

The screening procedure evaluates the following:

1. Propulsion hardware's compatibility with spacecraft wet mass;
2. Tsiolkovsky ΔV capability;
3. Nominal onboard trajectory-correction requirement;
4. v_∞ continuity;
5. Implemented flyby-turn feasibility;
6. Earth-entry speed for free-return trajectories;
7. Operational lifetime.

Propellant-capacity screening is supplemented by an analytical estimate of the required powered duration, as described in Section 5.5. This estimate identifies an additional necessary condition on the available manoeuvre time. Because continuous thrust arcs are not propagated, satisfaction of the capacity and aggregate time conditions does not establish finite-thrust trajectory feasibility.

4. Verification and Validation

The available source dataset consists of the original dissertation, reported numerical results, and the accompanying MATLAB implementation. No independent GMAT, STK/Astrogator, or equivalent n-body reconstruction was performed as part of the original study. Consequently, this section distinguishes carefully between internal numerical/physical verification and independent external validation. Only the former can be demonstrated from the available data.

4.1. Lambert-Solution and Conic Feasibility Checks

Every candidate transfer is generated from prescribed endpoint states and time-of-flight using the Lambert solver. Failed Lambert solutions are rejected. For converged solutions, the orbital angular momentum and eccentricity are calculated and used to determine the transfer-orbit periapsis. Solutions intersecting the central body are removed before entering the subsequent search stages. The same logic is retained inside the DE objective through the large invalid-solution penalty. These checks provide an internal consistency test that the accepted individual legs correspond to mathematically converged Lambert arcs that do not intersect the central body within the adopted two-body model. They should not, however, be interpreted as a benchmark verification of the Lambert implementation against an independent solver. Such a comparison would require either a published Lambert test case or an independent mission-analysis implementation and is outside the dataset available for the present paper.

4.2. Flyby v_∞ and Deflection Consistency

The principal internal verification of the multi-leg connections is the reduction in incoming/outgoing v_∞ mismatch after continuous refinement. For the EVME trajectory, the Venus mismatch is reduced from 0.993 km s^{-1} to 0.042 km s^{-1}, while the Mars mismatch is reduced from 3.348 km s^{-1} to 0.051 km s^{-1}. These reductions show that the DE refinement moves the initially coarse multi-leg seeds toward substantially more consistent unpowered-flyby conditions. For the Earth–Venus–Earth–Vesta trajectory, the corresponding absolute mismatch is reduced from 0.500 km s^{-1} to 0.010 km s^{-1} at Venus and from 0.868 km s^{-1} to 0.128 km s^{-1} at the Earth encounter. The implemented post-processing also compares the vector-based required turn angle in Equation (15) with the maximum turn available from Equation (16) wherever the corresponding intermediate-flyby check is invoked. Thus, retained trajectories satisfy both continuity and geometric checks implemented in the original software. For the Earth encounter preceding the final Vesta leg, the dissertation provides the optimized v_∞ mismatch but does not provide an independently propagated B-plane or periapsis solution. The present work therefore does not claim independent high-fidelity verification of that encounter.

4.3. Optimizer Refinement Evidence

The three test cases provide qualitatively different internal checks on optimizer behaviour. For EVME, the cascade filter produces 27 complete trajectories. DE substantially changes the encounter timing and reduces the two flyby v_∞ mismatches, indicating that the continuous refinement is not simply reproducing a grid point. For the Vesta transfer, the much larger search produces 2134 seed trajectories. DE reduces the overall mission duration from 1567 to 1538 days and substantially changes the distribution of time-of-flight between the individual legs while improving encounter continuity. For the Earth–Moon–Earth–Moon case, the reported encounter dates remain unchanged after DE refinement. This observation describes the timing outcome of the available run; it does not establish convergence of the grid or optimizer, nor does it exclude alternative candidates outside the explored region.

4.4. Grid Resolution and Seed-Population Adequacy

The reported searches use a one-day grid for the interplanetary cases and a half-day grid for the cislunar case. These are nominal search configurations; a controlled multi-resolution study has not been completed. The unchanged cislunar encounter dates after differential-evolution refinement describe the outcome of the reported run and do not establish grid convergence or adequate coverage of alternative solution regions. Likewise, the number of cascade candidates, the DE population size, and the random-number seed describe different aspects of the search and must not be treated interchangeably. No systematic retained-candidate-count study with common bounds, acceptance criteria, and computational budgets is reported. Consequently, the present results do not establish an optimal grid spacing, candidate count, or filtering threshold.

4.5. Scope and Limitations of Validation

The original study does not contain repeated DE runs with multiple random seeds, formal convergence-probability statistics, systematic perturbation of F and CR, or independent trajectory reconstruction in a second astrodynamics package. Such tests are common in more extensive global-optimization studies [13] and would strengthen the quantitative validation of the framework. Accordingly, the numerical results in this paper demonstrate internal consistency within the adopted patched-conic model and the implemented feasibility checks. They do not establish navigation-level trajectory accuracy. Future work should reconstruct at least one interplanetary solution using an independent

n-body mission-analysis tool and subsequently replace the impulsive propulsion screening with finite-thrust propagation.

5. Results and Discussion

5.1. Earth–Venus–Mars–Earth (EVME) Free-Return Mission

5.1.1. Mission Context and Lambert-Grid Search: Case EVME

The EVME mission is based on the class of Venus-assisted Mars free-return opportunities studied by Hughes et al. [32]. Free-return architectures are attractive for propulsion-constrained spacecraft because they avoid a major terminal orbit-insertion requirement. In the present small-satellite interpretation, the Venus encounter can additionally support atmospheric or ultraviolet measurements, while the Mars encounter can support imaging or environmental observations. CubeSat-class Venus mission concepts have previously been examined by NASA [33,34].

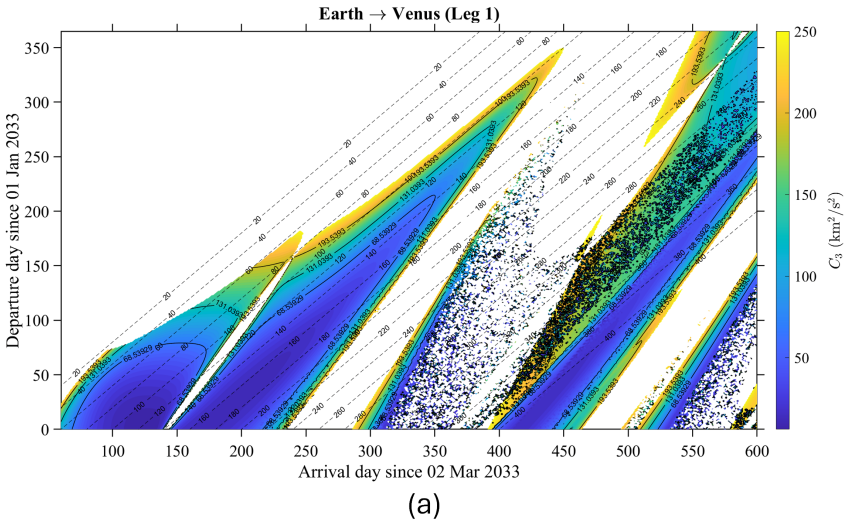
The Lambert-grid search for the EVME sequence is represented by the three porkchop diagrams in Figure 2. Figure 2a shows the Earth–Venus first-leg search. For a specified departure date, arrival date, and Lambert branch, the plotted departure characteristic energy is

$$C_{3,\mathrm{dep}} = \left\| \mathbf{v}_{\mathrm{L,dep}} - \mathbf{v}_E(t_{\mathrm{dep}}) \right\|^2, \tag{40}$$

where $\mathbf{v}_{\mathrm{L,dep}}$ is the heliocentric departure velocity obtained from the Lambert solution and $\mathbf{v}_E(t_{\mathrm{dep}})$ is the heliocentric velocity of Earth at the departure epoch. Both vectors are expressed in the same inertial reference frame. Velocity quantities are evaluated in km s^{-1}, giving departure C_3 in km^2 s^{-2}. The contours therefore represent the squared Earth-relative departure hyperbolic-excess speed. They do not represent the Venus arrival excess speed, a sum of departure and arrival speeds, or the onboard spacecraft manoeuvre requirement. The Venus arrival excess speed is a separate quantity calculated from Equation (9). The sampled minimum is defined over the accepted combinations of departure date, arrival date, and Lambert branch:

$$C_{3,\mathrm{grid,min}} = \min_{g \in \mathcal{G}_{\mathrm{acc}}} C_{3,\mathrm{dep}}(g), \tag{41}$$

where $\mathcal{G}_{\mathrm{acc}}$ contains the sampled combinations that satisfy the stated leg-level search conditions. Consequently, this minimum is conditional on the searched date domain, time-of-flight bounds, grid resolution, and evaluated Lambert branches. It is not a global minimum over unrestricted departure and arrival opportunities.



(a)

Figure 2. *Cont.*

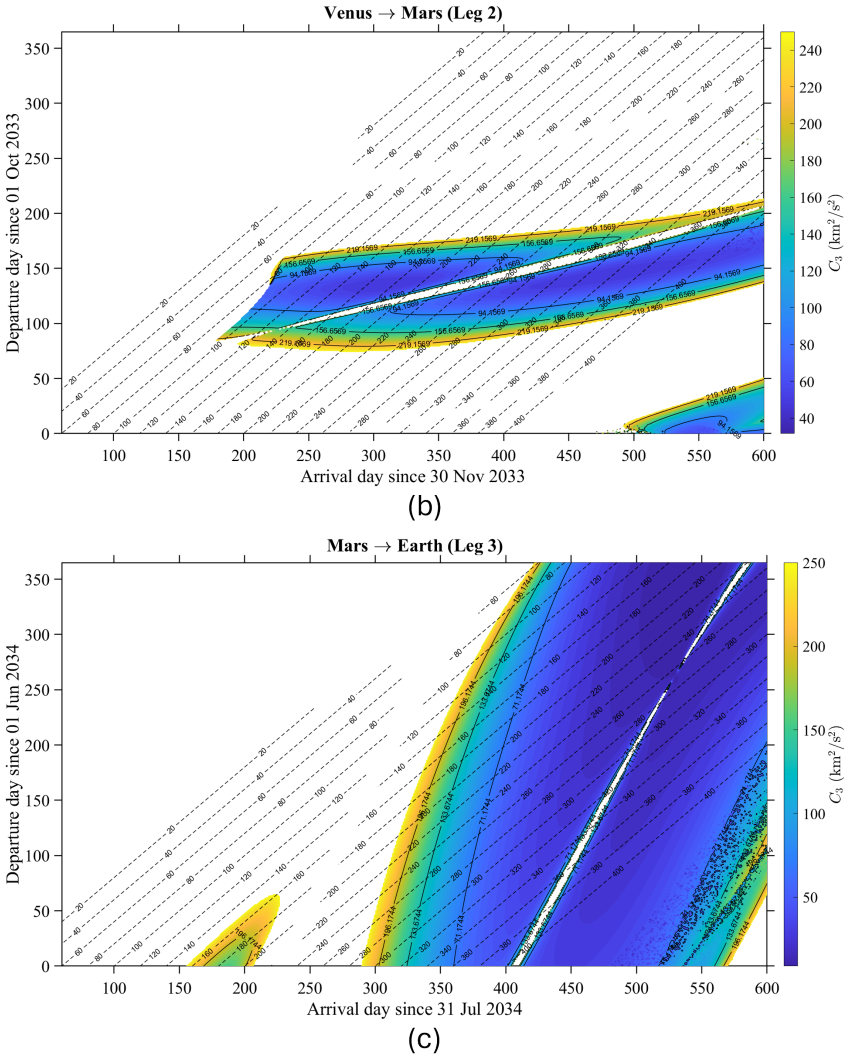


Figure 2. Lambert-grid departure-C_3 porkchop maps for the Earth–Venus–Mars–Earth sequence: (**a**) Earth–Venus; (**b**) Venus–Mars; (**c**) Mars–Earth. The horizontal axis represents arrival time, and the vertical axis represents departure time; each is expressed in days relative to the reference date printed on that axis. Colours indicate departure characteristic energy in km^2 s^{-2}, measured relative to the departing body of each leg. Dashed diagonal lines indicate constant times-of-flight in days. The maps describe the sampled search domains and do not establish unrestricted global minima. Arrival excess speed and onboard manoeuvre demand are separate quantities.

Figure 2b,c apply the same departure-energy definition to the Venus–Mars and Mars–Earth legs, respectively, using the velocity of the departing body for each leg. These maps provide candidate transfers for cascade filtering. A low-energy solution for an individual leg need not belong to an admissible complete EVME trajectory: the assembled sequence must also satisfy the encounter-matching, turning, launch, and Earth-return conditions.

5.1.2. Seed and Optimized Trajectories: Case EVME

The cascade filter produces 27 complete EVME trajectories. The best-ranked seed departs Earth on 7 June 2033 and returns on 12 November 2035, giving a total transfer duration of 886 days. The DE-refined solution departs Earth on 17 May 2033, encounters Venus on 4 February 2034 and Mars on 20 November 2034, and returns to Earth on 7 November 2035. The resulting duration is 902 days, or approximately 2.47 years. Although the total mission duration increases by 16 days relative to the best seed, the encounter consistency improves markedly. The Venus v_∞ mismatch decreases from 0.993 to 0.042 km s^{-1}, and

the Mars mismatch decreases from 3.348 to 0.051 km s^{-1}. The optimized first-leg C_3 increases from 13.106 to 19.247 km^2 s^{-2}. This behaviour is physically meaningful under the rideshare assumption: the optimizer accepts a more energetic launch condition because that energy is supplied by the launch system, while improved interplanetary geometry produces substantially better flyby continuity. The complete comparison of encounter epochs, individual-leg times-of-flight, characteristic energies, and flyby v_∞ mismatches before and after differential-evolution refinement is provided in Table 3.

Table 3. Comparison of the best cascade-filter seed and the differential-evolution-refined Earth–Venus–Mars–Earth (EVME) trajectory.

Parameter	Seed Trajectory	Optimized Trajectory
Earth departure	7 June 2033	17 May 2033
Venus flyby	27 February 2034	4 February 2034
Mars flyby	12 February 2035	20 November 2034
Earth return	12 November 2035	7 November 2035
Leg 1 TOF (days)	265	263
Leg 2 TOF (days)	351	288
Leg 3 TOF (days)	270	350
Total TOF (days)	886	902
Leg 1 C_3 (km^2 s^{-2})	13.106	19.247
Leg 2 C_3 (km^2 s^{-2})	50.048	56.387
Leg 3 C_3 (km^2 s^{-2})	13.080	21.320
Δv_∞ at Venus (km s^{-1})	0.993	0.042
Δv_∞ at Mars (km s^{-1})	3.348	0.051

Note: Δv_∞ denotes the absolute mismatch between the incoming and outgoing hyperbolic-excess-velocity magnitudes at the corresponding gravity-assist encounter.

5.1.3. Architecture Assessment: Case EVME

The 25 kg spacecraft equipped with the Busek BIT-3 is considered an illustrative configuration under the adopted launch, correction-budget, and lifetime assumptions. Using the propulsion inputs in Table 1, its ideal propellant-limited velocity-increment capacity is approximately 1.305 km s^{-1}. Relative to the nominal correction allowance of 0.10 km s^{-1}, the corresponding capacity margin is approximately 1.205 km s^{-1}.

This margin provides a basis for examining the configuration further but does not establish its superiority over alternative spacecraft–propulsion combinations. Under Equation (28), the configuration is assigned a 3.5-year screening lifetime. Compatibility with this assumption must be assessed alongside the corrected trajectory duration, encounter conditions, Earth-return requirements, and available manoeuvre windows.

The ideal powered duration associated with the nominal correction budget is approximately 26.24 days, as reported in Section 5.5. Its allocation among individual corrections requires a mission-specific manoeuvre schedule. Electrical-power availability, propulsion integration, tankage, thermal control, communications, radiation tolerance, reliability, attitude control, and payload allocation remain outside the present screening model.

Figures 3 and 4 present the propulsion-capacity and mission-duration dimensions of the assessment. These quantities support preliminary comparison, while acceptance of a complete EVME architecture requires satisfaction of the trajectory and spacecraft requirements together.

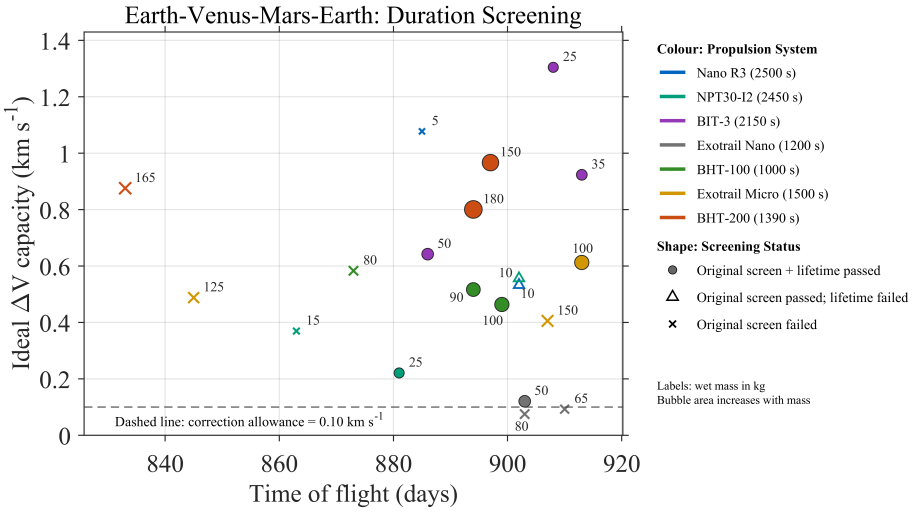


Figure 3. Combined propulsion and mission-duration screening for the optimized EVME trajectory.

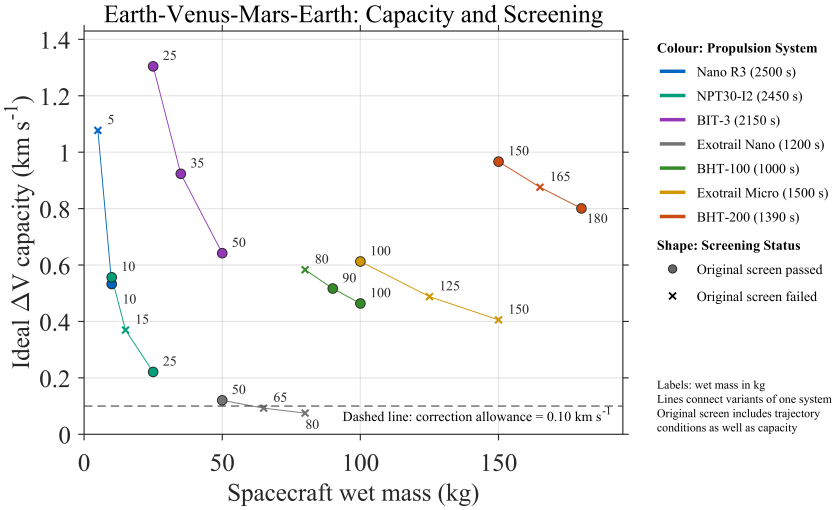


Figure 4. Propulsion ΔV capability across the spacecraft–propulsion architectures evaluated for the optimized EVME trajectory.

5.2. Earth–Moon–Earth–Moon (EMoEMo) Mission

5.2.1. Mission Context and Lambert-Grid Search: Case EMoEMo

The cislunar case is included to examine whether the same computational architecture can be applied in a geocentric domain and to a much shorter mission. It is not intended to reproduce the CAPSTONE trajectory. Rather, it is motivated by the broader use of low-energy and resonant cislunar dynamics demonstrated by missions such as EQUULEUS and CAPSTONE [35–37]. Recent research continues to examine low-thrust resonance gravity-assist design for lunar applications [19].

A 0.5-day grid is used because the Earth–Moon geometry varies substantially over a lunar orbital period. The first Earth–Moon transfer exhibits repeated low-energy departure windows separated by approximately one lunar month. The minimum signed energy indicator in the search is approximately $C_3^* = -2.168\,\mathrm{km^2\,s^{-2}}$, with candidate Earth–Moon transfer durations of approximately 2–10 days. Lunar arrival v_∞ values across the search window are approximately 0.87–1.80 $\mathrm{km\,s^{-1}}$. The second leg is a resonant geocentric arc with a prescribed time-of-flight range of approximately 20–40 days. The spacecraft follows a large Earth-centred ellipse before returning toward Earth. The third leg then connects

the Earth-return geometry to a second Moon encounter. The corresponding Lambert-grid energy maps are presented in Figure 5. The repeated Earth–Moon departure windows and the longer resonant intermediate leg are clearly distinguishable, illustrating the different dynamical character of the three cislunar transfer segments.

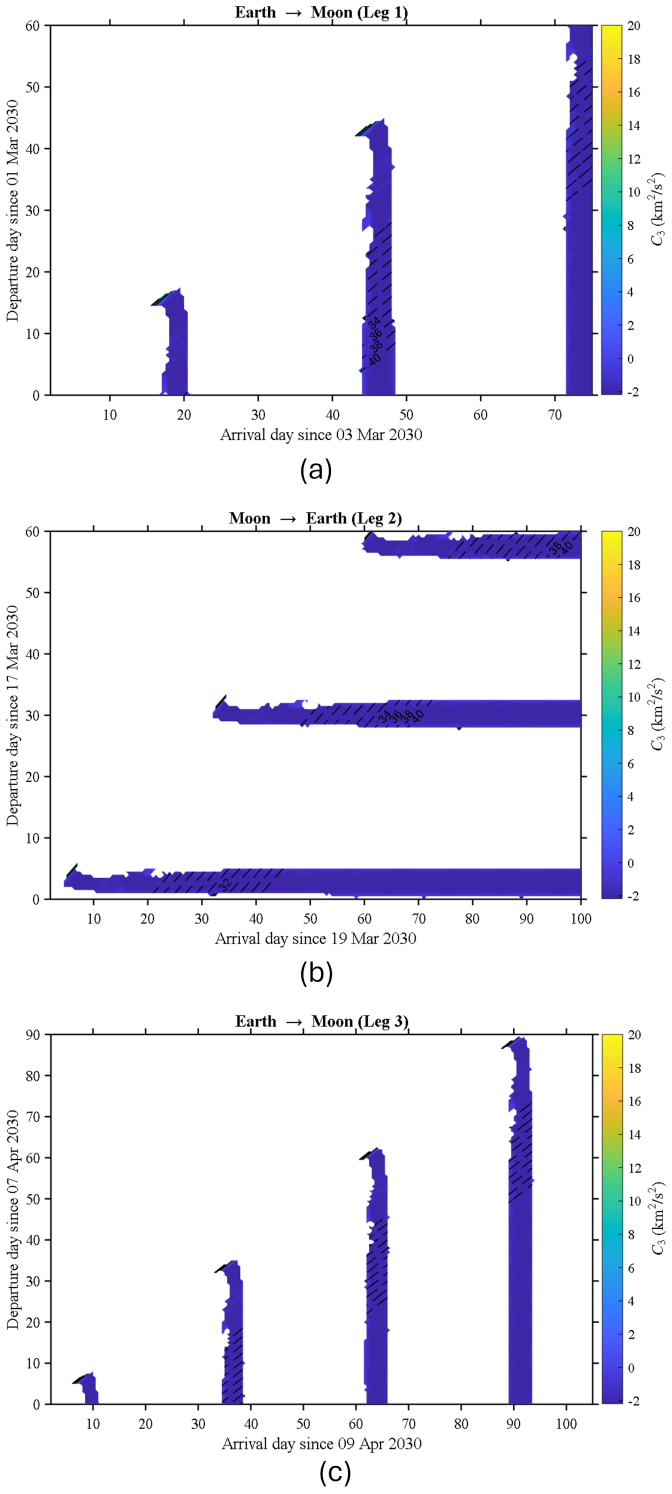


Figure 5. Lambert-grid energy maps for the Earth–Moon–Earth–Moon mission. (**a**) Earth–Moon first transfer; (**b**) resonant Moon–Earth leg; (**c**) Earth–Moon final transfer. Negative C_3^* values identify geocentrically bound solutions within the adopted two-body formulation.

5.2.2. Optimized Trajectory

The selected trajectory departs Earth on 14 March 2030 and reaches the Moon on 18 March 2030 after a 4.5-day transfer. It then follows a 23.5-day resonant arc and returns to Earth on 11 April 2030 before a final 5-day transfer to the Moon, arriving on 16 April 2030.

The total mission duration is$T_{\text{mission}} = 33$ days. The final signed energy indicators are $C_{3,1}^{*} = -2.120\ \text{km}^2\,\text{s}^{-2}$, $C_{3,2}^{*} = -0.866\ \text{km}^2\,\text{s}^{-2}$, and $C_{3,3}^{*} = -2.137\ \text{km}^2\,\text{s}^{-2}$. All remain negative, confirming a geocentrically bound solution within the adopted model. Unlike the interplanetary cases, the encounter epochs are unchanged by the DE stage. The 0.5-day Lambert grid has therefore already captured the relevant timing basin, leaving little continuous timing improvement for the optimizer. The seed and refined cislunar solutions are compared quantitatively in Table 4. The unchanged encounter epochs and total mission duration confirm that the 0.5-day Lambert grid had already identified the relevant timing basin, although the energy indicator of the resonant leg was refined by the continuous optimization.

Table 4. Comparison of the best cascade-filter seed and the differential-evolution-refined Earth–Moon–Earth–Moon trajectory.

Parameter	Seed Trajectory	Optimized Trajectory
Earth departure	14 March 2030	14 March 2030
First Moon encounter	18 March 2030	18 March 2030
Earth return	11 April 2030	11 April 2030
Second Moon encounter	16 April 2030	16 April 2030
Leg 1 TOF (days)	4.5	4.5
Leg 2 TOF (days)	23.5	23.5
Leg 3 TOF (days)	5.0	5.0
Total TOF (days)	33.0	33.0
Leg 1 C_3^{*} ($\text{km}^2\,\text{s}^{-2}$)	−2.120	−2.120
Leg 2 C_3^{*} ($\text{km}^2\,\text{s}^{-2}$)	−2.220	−0.866
Leg 3 C_3^{*} ($\text{km}^2\,\text{s}^{-2}$)	−2.148	−2.137

Note: C_3^{*} denotes the signed geocentric energy indicator used for the cislunar analysis. Negative values indicate that the spacecraft remains energetically bound to Earth within the adopted geocentric two-body formulation. The encounter dates and total mission duration remain unchanged after differential-evolution refinement.

5.2.3. Architecture Assessment: Case EMoEMo

The 5 kg spacecraft equipped with the ENPULSION Nano R3 is included as an illustrative low-mass configuration. Its ideal propellant-limited velocity-increment capacity is approximately $1.078\ \text{km}\,\text{s}^{-1}$, exceeding the nominal $0.10\ \text{km}\,\text{s}^{-1}$ correction allowance. The nominal 33-day mission duration is also below the adopted 1.5-year lifetime screening limit for this mass category.

However, the ideal powered duration required to deliver the nominal correction budget is approximately 16.50 days. As discussed in Section 5.5, this represents approximately half of the nominal mission duration before operational interruptions and manoeuvre-window restrictions are considered. Propellant capacity and the class-level lifetime assumption therefore provide insufficient evidence to establish operational feasibility.

The Nano R3 configuration is consequently retained as a comparison case rather than a demonstrated cislunar mission architecture. Its suitability depends on the ability to schedule and direct the required thrust arcs while satisfying the encounter conditions, power limitations, and spacecraft operational requirements. The present screening does not establish that a 5 kg spacecraft can execute the proposed mission.

Figures 6 and 7 illustrate the capacity and lifetime tests separately. Their interpretation must be combined with the manoeuvre-time assessment and subsequent dynamical verification.

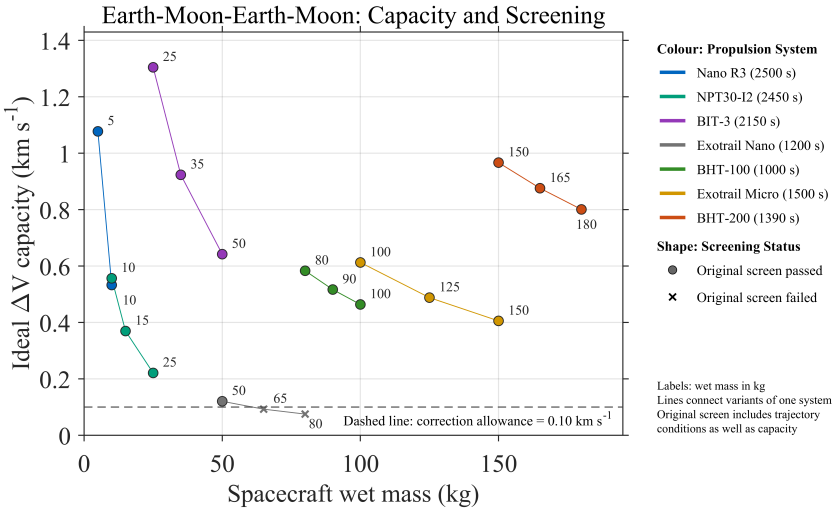


Figure 6. Propulsion screening for the 33-day Earth–Moon–Earth–Moon trajectory.

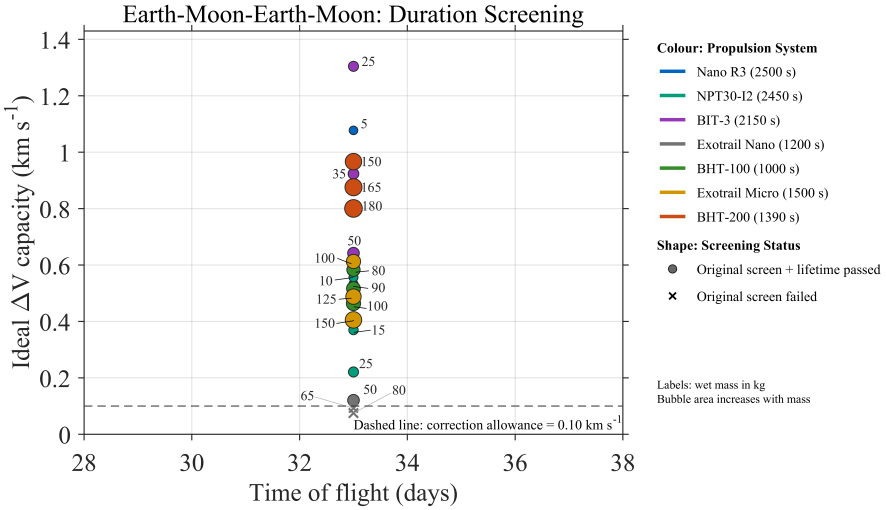


Figure 7. Lifetime screening for the 33-day Earth–Moon–Earth–Moon trajectory.

5.3. Earth–Venus–Earth–Vesta (EVE-Vesta) Mission

5.3.1. Mission Context and Lambert-Grid Search: Case EVE-Vesta

The Earth–Venus–Earth–Vesta case is the most ambitious trajectory examined. Vesta is a differentiated main-belt body whose structure and composition were extensively investigated by NASA's Dawn mission [38,39]. This case therefore provides a useful test of whether sequential inner-planet gravity assists can support a long-duration small-satellite transfer toward the main asteroid belt. Venus–Earth gravity-assist sequences are well established in interplanetary trajectory design [40], and repeated Venus/Earth assists formed a key part of the Galileo interplanetary trajectory [8]. Modern MGA sequence-generation research continues to exploit related energy-space and Tisserand-based methods [15].

The first Earth–Venus Lambert search identifies a low-energy basin centred near May 2031. Its minimum C_3 is approximately 6.17 $km^2\ s^{-2}$, corresponding to departure on 15 May 2031 and Venus arrival on 23 October 2031 after approximately 161 days. For the Venus–Earth leg, the minimum identified C_3 is approximately 7.68 $km^2\ s^{-2}$, although the complete multi-leg cascade selects a different portion of the search space in order to connect successfully with the final Vesta leg. The Earth–Vesta search is considerably narrower. Its minimum identified C_3 is approximately 30.1 $km^2\ s^{-2}$, for a transfer of approximately

906 days in the lowest-energy isolated-leg region. The narrowness of this window makes the complete mission particularly sensitive to the preceding Venus–Earth encounter geometry. The three Lambert-grid maps are shown in Figure 8. The comparatively narrow Earth–Vesta opportunity in Figure 8c is particularly important because it restricts the range of Venus–Earth trajectories that can subsequently connect to the final main-belt transfer.

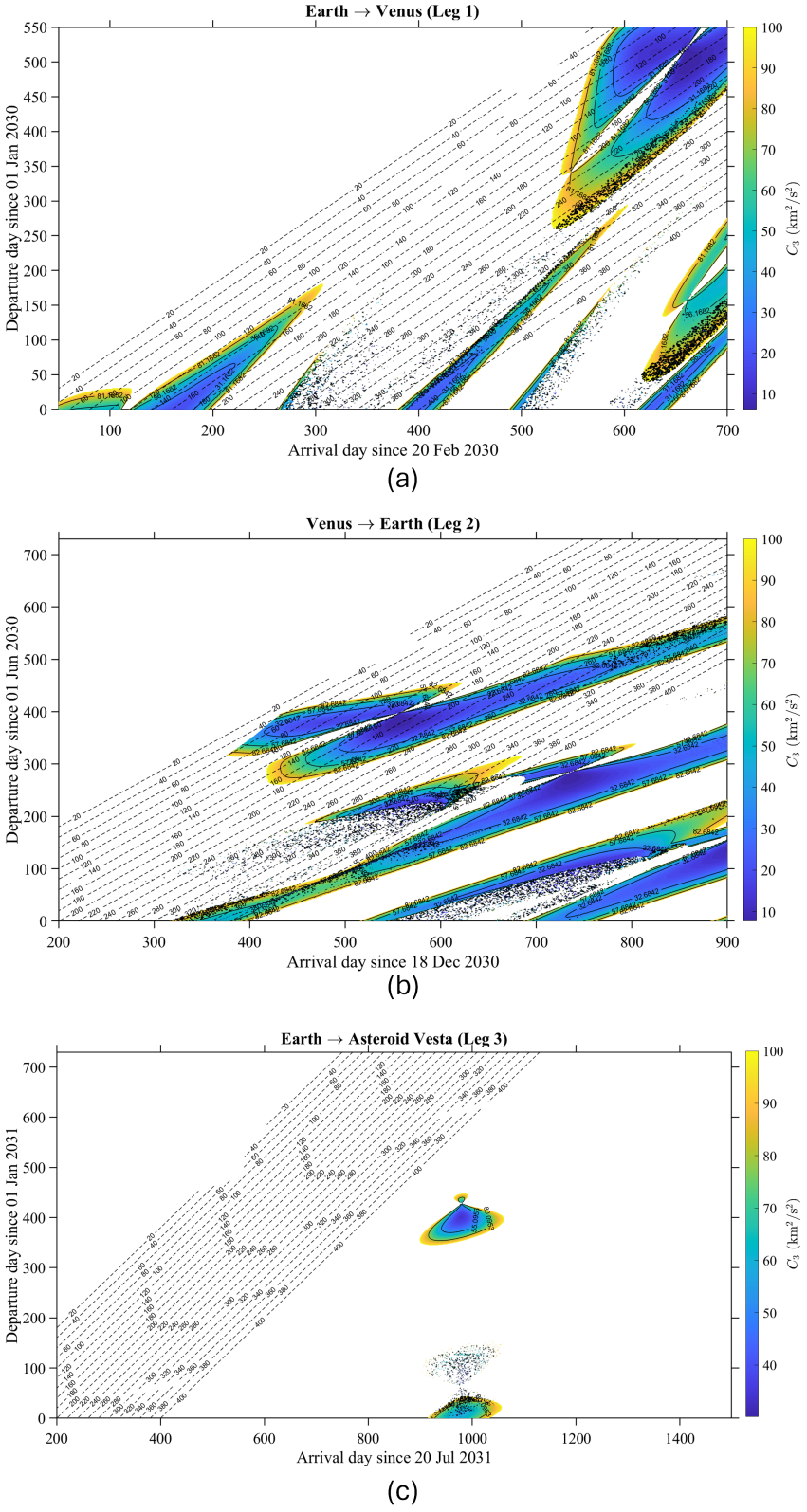


Figure 8. Lambert-grid energy maps for the Earth–Venus–Earth–Vesta trajectory.(**a**) Earth–Venus first transfer; (**b**) Venus–Earth leg; (**c**) Earth–Asteroid Vesta final transfer.

5.3.2. Seed and Optimized Trajectories: Case EVE-Vesta

The cascade filter produces 2134 complete seed trajectories. The best-ranked seed departs Earth on 31 May 2031 and reaches Vesta after 1567 days. DE refinement moves the departure to 27 May 2031.

The optimized encounter sequence is Earth → Venus → Earth → Vesta, with the Venus encounter on 14 September 2031, Earth encounter on 13 June 2032, and Vesta arrival on 12 August 2035. The final leg times-of-flight are $T_1 = 110$ days, $T_2 = 273$ days, $T_3 = 1155$ days, giving $T_{\text{mission}} = 1538$ days ≈ 4.21 years. The corresponding optimized characteristic energies are $C_{3,1} = 11.892$ km^2 s^{-2}, $C_{3,2} = 26.261$ km^2 s^{-2}, and $C_{3,3} = 84.851$ km^2 s^{-2}. The comparatively large third-leg value should not be interpreted as an onboard spacecraft burn. It represents the outgoing heliocentric-energy state associated with the Earth encounter and subsequent transfer to Vesta. The Venus v_∞ mismatch decreases from 0.500 to 0.010 km s^{-1}, while the Earth mismatch decreases from 0.868 to 0.128 km s^{-1}. These improvements demonstrate substantially stronger encounter continuity than in the original cascade seed. Table 5 provides the complete comparison between the best cascade-filter seed and the DE-refined trajectory, including the redistribution of time-of-flight between the three legs and the substantial reduction in v_∞ mismatch at both intermediate encounters.

Table 5. Comparison of the best cascade-filter seed and the differential-evolution-refined Earth–Venus–Earth–Vesta trajectory.

Parameter	Seed Trajectory	Optimized Trajectory
Earth departure	31 May 2031	27 May 2031
Venus flyby	17 November 2031	14 September 2031
Earth flyby	19 November 2031	13 June 2032
Vesta arrival	15 September 2035	12 August 2035
Leg 1 TOF (days)	170	110
Leg 2 TOF (days)	301	273
Leg 3 TOF (days)	1096	1155
Total TOF (days)	1567	1538
Leg 1 C_3 (km^2 s^{-2})	9.724	11.892
Leg 2 C_3 (km^2 s^{-2})	18.526	26.261
Leg 3 C_3 (km^2 s^{-2})	32.053	84.851
Δv_∞ at Venus (km s^{-1})	0.500	0.010
Δv_∞ at Earth (km s^{-1})	0.868	0.128

Note: Δv_∞ denotes the absolute mismatch between the incoming and outgoing hyperbolic-excess-velocity magnitudes at the corresponding gravity-assist encounter. The high Leg 3 C_3 of the optimized trajectory represents the heliocentric departure-energy state following the Earth gravity assist and is not an onboard spacecraft ΔV requirement.

5.3.3. Conditional Architecture Assessment

The 150 kg spacecraft equipped with the Busek BHT-200 is considered an illustrative configuration for the long-duration mission scenario. Its ideal propellant-limited velocity-increment capacity is approximately 0.967 km s^{-1}, giving a capacity margin of approximately 0.867 km s^{-1} above the nominal correction allowance. Its ideal powered duration for that allowance is approximately 13.31 days.

Under Equation (28), this configuration is assigned a six-year screening lifetime and, therefore, passes the lifetime condition for the fixed 1538-day benchmark. This outcome is conditional on the adopted lifetime model. As shown in Section 5.6, extending the nominal microsatellite lifetime boundary by approximately 20.3% removes the lifetime-only exclusion of that class for the same benchmark.

The nominal screening also does not uniquely identify the 150 kg BHT-200 configuration. For example, the 125 kg Exotrail Micro configuration is assigned the same six-year lifetime under the adopted mass-based rule and has an ideal velocity capacity of approximately 0.488 km s^{-1}. It therefore also passes the nominal capacity and benchmark lifetime tests. The BHT-200 configuration offers a larger capacity margin at a greater spacecraft mass, but a preferred architecture cannot be established without assessing the associated power, integration, manoeuvre-scheduling, and mission requirements.

The terminal transfer condition considered here is an encounter with Vesta. Rendezvous or orbit insertion would require an additional terminal-manoeuvre model and a corresponding revision of the onboard resource assessment. The present correction allowance must not be interpreted as including these additional requirements.

Figures 9 and 10 present the capacity and lifetime screening dimensions. Together with the sensitivity analysis, they support a conditional comparison of candidate configurations rather than a definitive selection of spacecraft mass or propulsion system.

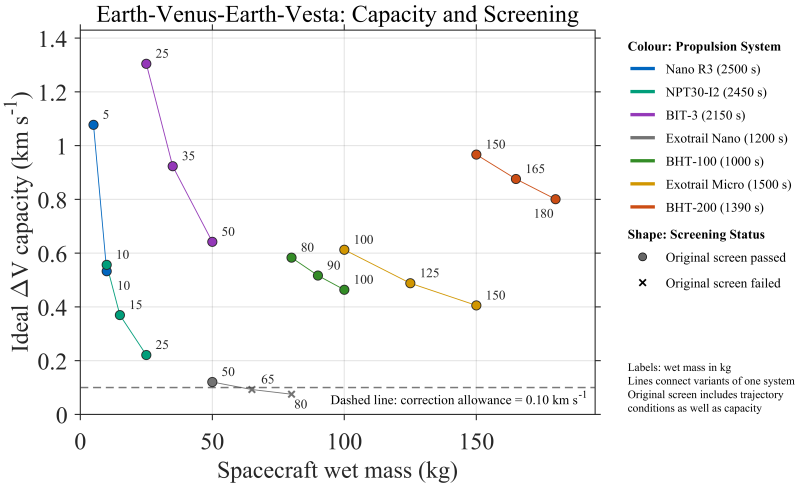


Figure 9. Propulsion screening for the Earth–Venus–Earth–Vesta trajectory.

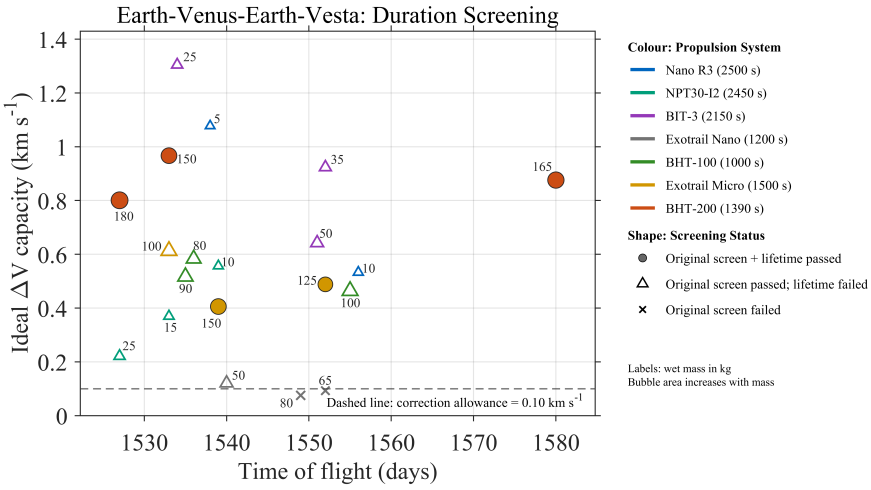


Figure 10. Mission-duration screening for the Earth–Venus–Earth–Vesta trajectory.

5.4. Sensitivity to the Onboard Correction Allowance

The influence of the assumed correction allowance is assessed independently of trajectory optimization using the adopted set of 20 spacecraft–propulsion configurations. For each configuration, the available velocity-increment budget is calculated using Equation (25), with the adopted spacecraft wet mass, available propellant mass, and specific impulse.

Under the baseline rideshare assumption, and with no additional deterministic manoeuvres included, the total onboard correction requirement is $2q$ for the two intermediate encounters. A configuration passes the propellant-capacity test when

$$\Delta V_{\text{budget}} \geq 2q. \tag{42}$$

Five values of q are considered, spanning one-half to ten times the nominal per-encounter allocation of 0.05 km s^{-1}. This range is used to examine how the passing architecture set changes as the assumed correction demand increases. The scenarios are sensitivity cases rather than statistical confidence bounds or correction requirements derived from a navigation-error analysis.

Table 6 presents the resulting capacity-compliant counts. At the nominal total correction budget of 0.10 km s^{-1}, 18 of the 20 configurations pass. Reducing the total budget to 0.05 km s^{-1} allows all 20 configurations to pass, whereas increasing it to 0.20 km s^{-1} and 0.40 km s^{-1} reduces the passing set to 17 and 15 configurations, respectively. At a total budget of 1.00 km s^{-1}, only two configurations retain sufficient ideal propellant capacity.

Table 6. Sensitivity of propellant-capacity compliance to the assumed onboard correction allowance for the 20 evaluated spacecraft–propulsion configurations.

Per-Encounter Allowance q (km s^{-1})	Total Correction Budget $2q$ (km s^{-1})	Configurations Passing Capacity Test
0.025	0.05	20/20
0.050	0.10	18/20
0.100	0.20	17/20
0.200	0.40	15/20
0.500	1.00	2/20

Note: Passing counts represent compliance with Equation (42) only. They exclude encounter geometry, operational lifetime, available electrical power, manoeuvre scheduling, and finite-thrust trajectory constraints.

The results demonstrate that the nominal passing count depends materially on the assumed onboard correction requirement. Because this isolated assessment uses the same propulsion dataset and correction budget for each mission, it does not distinguish between their navigation difficulty or dynamical feasibility. Mission-specific correction requirements and any deterministic manoeuvres must be assessed separately before the architecture counts can support mission-level conclusions.

5.5. Ideal Thrust Duration and Manoeuvre-Time Limitations

Sufficient propellant capacity does not establish that a propulsion system can deliver the required velocity increment within the available manoeuvre windows. An additional analytical assessment therefore estimates the powered duration associated with the adopted correction budget.

For constant thrust T and specific impulse I_{sp}, the ideal propellant requirement is

$$m_{\text{prop,req}} = m_0 \left[1 - \exp\left(-\frac{\Delta V}{I_{\text{sp}} g_0} \right) \right], \tag{43}$$

where m_0 is the spacecraft wet mass before the manoeuvre. The corresponding powered duration is

$$t_{\text{on}} = \frac{m_{\text{prop,req}} I_{\text{sp}} g_0}{T}. \tag{44}$$

For these equations, consistent SI units are used: ΔV is expressed in $\mathrm{m\,s^{-1}}$, $g_0 = 9.80665\ \mathrm{m\,s^{-2}}$, mass in kilograms, and thrust in newtons, giving t_{on} in seconds. The baseline correction budget of $0.10\ \mathrm{km\,s^{-1}}$ therefore corresponds to $\Delta V = 100\ \mathrm{m\,s^{-1}}$.

These expressions assume constant propulsion performance and neglect steering losses, interruptions, and restrictions on the placement of thrust arcs. They estimate the propellant consumption and powered duration associated with a prescribed scalar velocity-increment budget; they do not propagate a finite-thrust trajectory or demonstrate delivery of the required encounter state.

Using the propulsion inputs in Table 1, the ideal powered durations for three illustrative configurations are reported in Table 7. These calculations are independent of the trajectory-search objective.

Table 7. Ideal powered duration required to deliver a total velocity increment of $100\ \mathrm{m\,s^{-1}}$ using the adopted constant-thrust and constant-specific-impulse assumptions.

Propulsion System	Initial Spacecraft Wet Mass (kg)	Ideal Powered Duration (Days)
ENPULSION Nano R3	5	16.50
Busek BIT-3	25	26.24
Busek BHT-200	150	13.31

Note: Powered duration excludes interruptions and scheduling restrictions. The configurations are illustrative screening cases and are not established mission architectures.

If t_{window} denotes the cumulative duration of permitted manoeuvre windows and f_{duty} is the assumed operating duty fraction within those windows, a necessary aggregate time condition is

$$t_{\mathrm{on}} \leq f_{\mathrm{duty}} t_{\mathrm{window}}, \qquad 0 < f_{\mathrm{duty}} \leq 1. \tag{45}$$

The permitted windows must account for restrictions arising from power availability, spacecraft attitude, communications, navigation operations, and encounter proximity. Total mission duration is therefore not equivalent to available thrusting time. Satisfying Equation (45) is also insufficient by itself: the individual manoeuvres must be appropriately timed and directed to achieve their required trajectory corrections.

For the nominal 33-day cislunar case, the 5 kg Nano R3 configuration requires approximately 16.50 days of ideal powered operation, corresponding to approximately half of the mission duration. This is a substantial scheduling requirement even before operational interruptions are considered. Consequently, the configuration cannot be described as operationally feasible on the basis of propellant capacity alone. Its suitability requires an explicit manoeuvre schedule and finite-thrust trajectory assessment.

5.6. Sensitivity to Operational-Lifetime Assumptions

The influence of the assumed lifetime boundaries is examined using a fixed duration benchmark of 1538 days, corresponding to approximately 4.211 years when a year is taken as 365.25 days. This benchmark isolates the effect of the lifetime assumptions from the trajectory search. Its use does not independently validate the Vesta trajectory or establish its final mission duration.

The nominal limits in Equation (28) are varied using a common multiplier α:

$$L_\alpha(m_0) = \alpha L_0(m_0). \tag{46}$$

Five scenarios are considered: $\alpha = 0.50$, 0.75, 1.00, 1.25, and 1.50. These represent changes of up to 50% below and above the nominal limits. They are parameter-sensitivity scenarios, rather than statistical uncertainty intervals or reliability predictions.

For each scenario, a configuration is retained in the joint capacity-and-lifetime assessment when

$$\Delta V_{\text{budget}} \geq 0.10 \text{ km s}^{-1}, \qquad L_{\alpha}(m_0) \geq T_{\text{b}}, \tag{47}$$

where $T_{\text{b}} = 1538/365.25$ yr is the fixed benchmark duration. The assessment uses the same 20 spacecraft–propulsion configurations as the correction-budget sensitivity analysis. Table 8 summarises the number of configurations satisfying both the propellant-capacity and assumed-lifetime conditions for each lifetime multiplier.

Table 8. Sensitivity of joint propellant-capacity and lifetime compliance to the assumed lifetime limits, for a fixed 1538-day benchmark and a total correction budget of 0.10 km s^{-1}.

Lifetime Multiplier, α	Configurations Passing Both Tests
0.50	0/20
0.75	5/20
1.00	5/20
1.25	15/20
1.50	15/20

Note: The multiplier is applied simultaneously to all three nominal lifetime limits. Passing counts include only the propellant-capacity and assumed-lifetime conditions in Equation (47); encounter geometry, electrical-power availability, and finite-thrust constraints require separate assessment.

At the nominal lifetime limits, five configurations satisfy both conditions. Reducing the limits by 25% preserves these five configurations, whereas a 50% reduction excludes all configurations. Increasing the limits by 25% expands the passing set to 15 configurations, with no further increase at the 50% extension considered here.

The microsatellite lifetime boundary is particularly influential. For the fixed benchmark, the nominal 3.5-year limit must increase by approximately

$$100\left(\frac{1538/365.25}{3.5} - 1\right) = 20.31\% \tag{48}$$

before lifetime alone ceases to exclude this class. Propellant capacity and the other mission constraints can still exclude individual configurations after this lifetime condition is met.

Consequently, the apparent preference for larger spacecraft in the long-duration case is conditional on the adopted lifetime boundaries. The results support interpreting the active screening constraint as a property of the mission scenario and its assumptions. They do not establish a universal migration from propulsion-limited to lifetime-limited mission design.

5.7. Cross-Mission Comparison

The comparison in Table 9 is interpreted in terms of mission-dependent screening outcomes under the adopted assumptions. Encounter geometry, onboard correction demand, available manoeuvre time, and operational lifetime impose distinct requirements whose relative importance depends on the mission scenario. The sensitivity analyses in Sections 5.4 and 5.6 demonstrate that the passing architecture set changes with the correction allocation and lifetime boundaries. The powered-duration assessment in Section 5.5 further shows why a short mission can remain operationally challenging despite adequate propellant capacity. Accordingly, any change in the active screening constraint across the three cases is conditional on the stated model assumptions and does not establish a general ordering of the constraints governing small-satellite missions.

The three configurations highlighted in the cross-mission comparison were chosen to illustrate distinct properties of the evaluated 20-configuration set, rather than through a common optimization criterion for spacecraft selection. For EVME, the 25 kg Busek BIT-3 configuration illustrates the largest ideal velocity-increment capacity in the evaluated set

(approximately 1.305 km s^{-1}) under the adopted propellant and specific-impulse inputs. Its inclusion does not imply that it is the lowest-mass configuration capable of satisfying the nominal correction allowance.

Table 9. Illustrative spacecraft–propulsion configurations for the three mission contexts. Capacity margins are measured relative to the nominal total correction allowance of 0.10 km s^{-1}.

Mission Case	Illustrative Configuration	Velocity Capacity (km s^{-1})	Capacity Margin (km s^{-1})
EVME	25 kg Busek BIT-3	1.305	1.205
Cislunar	5 kg ENPULSION Nano R3	1.078	0.978
Vesta	150 kg Busek BHT-200	0.967	0.867

Note: Capacities are calculated from the adopted propulsion inputs and spacecraft wet masses using Equation (25). The configurations are illustrative comparison cases. The table does not establish trajectory, finite-thrust, or complete spacecraft feasibility, and it does not identify a unique or optimal architecture.

For the cislunar case, the 5 kg ENPULSION Nano R3 configuration illustrates the lowest evaluated spacecraft mass. Its calculated capacity of approximately 1.078 km s^{-1} exceeds the nominal correction allowance, and the 33-day benchmark is within its assumed screening lifetime. However, the ideal powered duration reported in Section 5.5 shows that these conditions alone do not establish the operational feasibility of the required manoeuvres.

For the Vesta case, the 150 kg Busek BHT-200 configuration illustrates the largest calculated velocity-increment capacity among the five configurations satisfying both the nominal correction-capacity test and the assumed lifetime condition for the fixed 1538-day benchmark. Its capacity is approximately 0.967 km s^{-1}, and its assigned screening lifetime is six years. It is not the lowest-mass passing configuration: the 125 kg Exotrail Micro alternative also satisfies these two tests but provides a smaller capacity of approximately 0.488 km s^{-1}.

These examples therefore illustrate capacity margin, low spacecraft mass, and capacity within the lifetime-compliant subset, respectively. They do not constitute a ranking based on a common system-level objective. A final architecture selection would additionally require assessment of electrical power, propulsion integration, thermal control, communications, reliability, payload allocation, and finite-thrust manoeuvre scheduling.

Two broader observations follow: First, the value of a gravity-assist architecture should not be assessed solely by minimizing Earth-departure C_3. The EVME solution deliberately accepts a higher launch-energy state than the best cascade seed because it provides dramatically improved downstream encounter compatibility. Under rideshare injection, this additional energy is external to the spacecraft propulsion budget. Second, the propulsion trade study does not support a universal minimum-I_{sp} threshold for deep-space small satellites. It shows only that, within the particular propulsion systems, propellant masses, spacecraft masses, and fixed 0.10 km s^{-1} correction allocation evaluated here, the two 65 and 80 kg Exotrail Nano combinations fail the Tsiolkovsky screen in all three mission cases. Generalizing this result to all SmallSat propulsion systems would be inappropriate, particularly given the rapid evolution of electric-propulsion technology [4] and the current NASA technology survey [5]. The active screening constraint depends on the adopted mission scenario and system assumptions. The correction-budget and lifetime sensitivity assessments show that changing these assumptions can alter the passing configuration set. This supports integrated trajectory–spacecraft screening during preliminary design, without establishing a universal progression from propulsion-limited to lifetime-limited missions.

6. Conclusions

This study presents an integrated preliminary-design workflow linking Lambert-grid exploration, cascade filtering, and differential-evolution refinement with explicit launch, encounter, propulsion, mass, and operational-lifetime assumptions. Its contribution is the coordinated application of established methods to examine candidate multi-gravity-assist missions and their spacecraft-level implications. The analytical sensitivity assessment shows that increasing the total correction allowance from 0.10 to 0.40 km s^{-1} reduces the number of capacity-compliant configurations from 18 to 15 out of 20. For the fixed 1538-day benchmark, extending the assumed 3.5-year microsatellite lifetime by approximately 20.3% removes its lifetime-only exclusion. Furthermore, the 16.50-day ideal powered duration calculated for the 5 kg Nano R3 configuration demonstrates why propellant capacity alone cannot establish operational feasibility for the 33-day cislunar benchmark. These results show that the candidate architecture set depends materially on the adopted screening assumptions. The highlighted configurations are therefore illustrative cases for further assessment, rather than established mission architectures. The framework employs patched-conic dynamics and a trajectory-search surrogate, and it does not establish minimum propellant consumption, global optimality, or finite-thrust feasibility. Independent dynamical reconstruction, stochastic robustness assessment, navigation-based correction budgets, and explicit power and manoeuvre-scheduling models remain necessary before the candidate trajectories and configurations can support mission-level design decisions.

Author Contributions: Conceptualization, S.D. and N.P.; methodology, S.D. and N.P.; software, S.D.; validation, S.D.; formal analysis, S.D.; investigation, S.D.; writing—original draft preparation, S.D.; writing—review and editing, N.P.; supervision, N.P. All authors have read and agreed to the published version of the manuscript.

Funding: This research received no external funding

Institutional Review Board Statement: Not applicable.

Informed Consent Statement: Not applicable.

Data Availability Statement: The original contributions presented in this study are included in the article. Further inquiries can be directed to the corresponding author.

Conflicts of Interest: The authors declare no conflicts of interest.

Abbreviations

The following abbreviations are used in this manuscript:

CAPSTONE	Cislunar Autonomous Positioning System Technology Operations and Navigation Experiment
DE	Differential Evolution
EVME	Earth–Venus–Mars–Earth
FEEP	Field-Emission Electric Propulsion
GMAT	General Mission Analysis Tool
JPL	Jet Propulsion Laboratory
MarCO	Mars Cube One
MGA	Multi-Gravity Assist
NASA	National Aeronautics and Space Administration
RF	Radio Frequency
STK	Systems Tool Kit
TCM	Trajectory Correction Manoeuvre
TOF	Time-of-Flight

References

1. Millan, R.M.; von Steiger, R.; Ariel, M.; Bartalev, S.; Borgeaud, M.; Campagnola, S.; Castillo-Rogez, J.C.; Fléron, R.; Gass, V.; Gregorio, A.; et al. Small satellites for space science: A COSPAR scientific roadmap. *Adv. Space Res.* **2019**, *64*, 1466–1517. [CrossRef]
2. Bouzoukis, K.P.; Moraitis, G.; Kostopoulos, V.; Lappas, V. An Overview of CubeSat Missions and Applications. *Aerospace* **2025**, *12*, 550. [CrossRef]
3. Klesh, A.; Clement, B.; Colley, C.; Essmiller, J.; Forgette, D.; Krajewski, J.; Marinan, A.; Martin-Mur, T.; Steinkraus, J.; Sternberg, D.; et al. MarCO: Early Operations of the First CubeSats to Mars. In Proceedings of the 32nd Annual AIAA/USU Conference on Small Satellites, Logan, UT, USA, 4–9 August 2018; Paper SSC18-WKIX-04. Available online: https://digitalcommons.usu.edu/smallsat/2018/all2018/474/ (accessed on 16 March 2026).
4. Alnaqbi, S.; Darfilal, D.; Swei, S.S.M. Propulsion Technologies for CubeSats: Review. *Aerospace* **2024**, *11*, 502. [CrossRef]
5. NASA Small Spacecraft Systems Virtual Institute. State-of-the-Art of Small Spacecraft Technology. Technical Report. National Aeronautics and Space Administration. 2026. 2026 Edition. Available online: https://www.nasa.gov/smallsat-institute/sst-soa/ (accessed on 13 August 2026).
6. Cesarone, R.J. A Gravity Assist Primer. *AIAA Stud. J.* **1989**, *27*, 16–22. Available online: https://ntrs.nasa.gov/citations/19890063851 (accessed on 16 March 2026).
7. Lutz, O. Then There Were Two: Voyager 2 Reaches Interstellar Space. NASA Jet Propulsion Laboratory. 2018. Available online: https://www.jpl.nasa.gov/edu/resources/teachable-moment/then-there-were-two-voyager-2-reaches-interstellar-space/ (accessed on 13 August 2026).
8. D'Amario, L.A.; Bright, L.E.; Wolf, A.A. Galileo trajectory design. *Space Sci. Rev.* **1992**, *60*, 23–78. [CrossRef]
9. Vasile, M.; De Pascale, P. Preliminary Design of Multiple Gravity-Assist Trajectories. *J. Spacecr. Rocket.* **2006**, *43*, 794–805. [CrossRef]
10. Vallado, D.A. *Fundamentals of Astrodynamics and Applications*, 4th ed.; Microcosm Press: Hawthorne, CA, USA, 2013.
11. Li, J.; Zhao, J.; Li, F. A new method of patched-conic for interplanetary orbit. *Optik* **2018**, *156*, 121–127. [CrossRef]
12. Izzo, D.; Becerra, V.M.; Myatt, D.R.; Nasuto, S.J.; Bishop, J.M. Search space pruning and global optimisation of multiple gravity assist spacecraft trajectories. *J. Glob. Optim.* **2007**, *38*, 283–296. [CrossRef]
13. Song, Y.; Wu, W.; Hu, H.; Lin, M.; Wang, H.; Zhang, J. Gravity assist space pruning and global optimization of spacecraft trajectories for solar system boundary exploration. *Complex Intell. Syst.* **2024**, *10*, 323–341. [CrossRef]
14. Gavira-Aladro, M.; Bombardelli, C. Lambert-Free Solution of Multiple-Gravity-Assist Optimization Problem. *J. Guid. Control Dyn.* **2024**, *47*, 1822–1838. [CrossRef]
15. Li, Z.; Wang, Y.; Koryanov, V. Trajectory design for comet 67P/Churyumov–Gerasimenko mission: Multiple gravity assist analysis using Tisserand Graph. *Astrodynamics* **2026**, *10*, 239–259. [CrossRef]
16. Morante, D.; Sanjurjo Rivo, M.; Soler, M. A Survey on Low-Thrust Trajectory Optimization Approaches. *Aerospace* **2021**, *8*, 88. [CrossRef]
17. Maiwald, V. Optimization of Low-Thrust Gravity-Assist Trajectories Under Application of Tisserand's Criterion. Ph.D. Thesis, University of Bremen, Bremen, Germany, 2018. Available online: https://elib.dlr.de/121821/ (accessed on 21 April 2026).
18. Hofmann, C.; Topputo, F. Convex Low-Thrust Trajectory Optimization with No-Thrust Constraints and Moving Target. *J. Spacecr. Rocket.* **2024**, *61*, 889–899. [CrossRef]
19. Lee, J.; Ahn, J. Low-Thrust Resonance Gravity-Assist Trajectory Design for Lunar Missions. *J. Spacecr. Rocket.* **2024**, *61*, 1074–1083. [CrossRef]
20. Vasiloff, K.; Adesina, I.; Wang, Z.; Mall, K.; DeLaurentis, D.A. Trajectory Optimization for Orbit Transfers: Principles, Advances, Case Studies, and Outlook. *Aerospace* **2025**, *12*, 1087. [CrossRef]
21. Storn, R.; Price, K. Differential Evolution—A Simple and Efficient Heuristic for Global Optimization over Continuous Spaces. *J. Glob. Optim.* **1997**, *11*, 341–359. [CrossRef]
22. Bottiglieri, C.; Piccolo, F.; Giordano, C.; Ferrari, F.; Topputo, F. Applied Trajectory Design for CubeSat Close-Proximity Operations around Asteroids: The Milani Case. *Aerospace* **2023**, *10*, 464. [CrossRef]
23. Topputo, F.; Zhang, C. Survey of Direct Transcription for Low-Thrust Space Trajectory Optimization with Applications. *Abstr. Appl. Anal.* **2014**, *2014*, 851720. [CrossRef]
24. Ito, D.; Pushparaj, N.; Kawakatsu, Y. Expanding Interplanetary Transfer Opportunities from Geostationary Transfer Orbits via Earth Synchronous Orbits. *J. Spacecr. Rocket.* **2023**, *60*, 79–94. [CrossRef]
25. ENPULSION. Nano R^3: Compact Satellite Propulsion. Available online: https://www.enpulsion.com/products/nano-r3/ (accessed on 20 April 2026).
26. ThrustMe. NPT30-I2 Ion Propulsion System. Available online: https://www.thrustme.fr/products/npt30-i2 (accessed on 20 April 2026).
27. Busek Co. Inc. BIT-3 RF Ion Thruster. Available online: https://www.busek.com/bit3 (accessed on 20 April 2026).

28. Exotrail. Hall Thrusters: Spaceware. Available online: https://www.exotrail.com/product/hall-thrusters-spaceware (accessed on 13 September 2026).
29. Busek Co. Inc. BHT-100 Hall Effect Thruster. Available online: https://www.busek.com/bht100-hall-thruster (accessed on 20 April 2026).
30. Busek Co. Inc. BHT-200 Hall Effect Thruster. Available online: https://www.busek.com/bht200 (accessed on 20 April 2026).
31. Rafalskyi, D.; Martínez Martínez, J.; Habl, L.; Aanesland, A. Development and In-Flight Testing of an Iodine Ion Thruster. In Proceedings of the 35th Annual Small Satellite Conference, Logan, UT, USA, 7–12 August 2021; Paper SSC21-XI-04. Available online: https://digitalcommons.usu.edu/smallsat/2021/all2021/207/ (accessed on 21 April 2026).
32. Hughes, K.M.; Edelman, P.J.; Saikia, S.J.; Longuski, J.M.; Loucks, M.E.; Carrico, J.P., Jr.; Tito, D.A. Fast Free Returns to Mars and Venus with Applications to Inspiration Mars. *J. Spacecr. Rocket.* **2015**, *52*, 1712–1735. [CrossRef]
33. Keesey, L. NASA Studies CubeSat Mission to Solve Venusian Mystery. NASA Goddard Space Flight Center. 2017. Available online: https://www.nasa.gov/technology/nasa-studies-cubesat-mission-to-solve-venusian-mystery/ (accessed on 5 April 2026).
34. NASA Jet Propulsion Laboratory. NASA Selects CubeSat, SmallSat Mission Concept Studies. 2017. Available online: https://www.jpl.nasa.gov/news/nasa-selects-cubesat-smallsat-mission-concept-studies/ (accessed on 5 April 2026).
35. Funase, R.; Ikari, S.; Miyoshi, K.; Kawabata, Y.; Nakajima, S.; Nomura, S.; Funabiki, N.; Ishikawa, A.; Kakihara, K.; Matsushita, S.; et al. Mission to Earth–Moon Lagrange Point by a 6U CubeSat: EQUULEUS. *IEEE Aerosp. Electron. Syst. Mag.* **2020**, *35*, 30–44. [CrossRef]
36. Gardner, T.; Cheetham, B.; Forsman, A.; Meek, C.; Kayser, E.; Parker, J.; Thompson, M.; Latchu, T.; Rogers, R.; Bryant, B.; et al. CAPSTONE: A CubeSat Pathfinder for the Lunar Gateway Ecosystem. In Proceedings of the 35th Annual Small Satellite Conference, Logan, UT, USA, 7–12 August 2021. Available online: https://digitalcommons.usu.edu/smallsat/2021/all2021/142/ (accessed on 21 April 2026).
37. National Aeronautics and Space Administration. What is CAPSTONE? 2026. Updated 26 June 2026. Available online: https://www.nasa.gov/smallspacecraft/capstone/ (accessed on 13 August 2026)
38. Russell, C.T.; Raymond, C.A.; Coradini, A.; McSween, H.Y.; Zuber, M.T.; Nathues, A.; De Sanctis, M.C.; Jaumann, R.; Konopliv, A.S.; Preusker, F.; et al. Dawn at Vesta: Testing the Protoplanetary Paradigm. *Science* **2012**, *336*, 684–686. [CrossRef] [PubMed]
39. Rayman, M.D.; Fraschetti, T.C.; Raymond, C.A.; Russell, C.T. Dawn: A mission in development for exploration of main belt asteroids Vesta and Ceres. *Acta Astronaut.* **2006**, *58*, 605–616. [CrossRef]
40. Strange, N.J.; Longuski, J.M. Graphical Method for Gravity-Assist Trajectory Design. *J. Spacecr. Rocket.* **2002**, *39*, 9–16. [CrossRef] [PubMed]

Disclaimer/Publisher's Note: The statements, opinions and data contained in all publications are solely those of the individual author(s) and contributor(s) and not of MDPI and/or the editor(s). MDPI and/or the editor(s) disclaim responsibility for any injury to people or property resulting from any ideas, methods, instructions or products referred to in the content.